Journal of Computational Physics (2022)

Contents lists available at ScienceDirect

Journal of Computational Physics

journal homepage: www.elsevier.com/locate/jcp

A weak coupling between a near-wall Eulerian solver and a Vortex Particle-Mesh method for the efficient simulation of 2D external flows

P. Billuart[a,*], M. Duponcheel[a], G. Winckelmans[a], P. Chatelain[a]

[a]*Institute of Mechanics, Materials and Civil Engineering, Université catholique de Louvain, 1348 Louvain-la-Neuve, Belgium*

ARTICLE INFO

Article history:
Received 17 September 2021

Coupled method, Body-fitted solver, Vortex Particle-Mesh method, Incompressible external flows

ABSTRACT

We introduce and validate a weak coupling approach between a body-fitted velocity-pressure solver and a Vortex Particle-Mesh (VPM) method in 2D for the simulation of incompressible external aerodynamics. The approach does not involve inner iterations, conserves circulation up to interpolation accuracy without resorting to a panel method, and accommodates different time steps across the solvers. It also utilizes a mixed boundary condition for the body-fitted solver that ensures the continuity of the vorticity field across the solvers. The second order convergence of the methodology is first demonstrated. We then assess it on the flow past a cylinder at various Reynolds numbers (from $Re = 550$ to 9500), and we finally apply it to the flow past an airfoil at $Re = 5000$.

© 2022 Elsevier Inc. All rights reserved.

1. Introduction

Numerical simulations of flows past immersed objects are ubiquitous in both research and industry, spanning e.g. vehicle aero- or hydrodynamics, biological propulsion, wind energy, civil engineering, etc. The targeted problems remain quite challenging as they usually require high accuracy and thus entail considerable computational costs. This challenge is even exacerbated for problems where the device, or the animal, interacts with either its own or another device's wake. This indeed imposes the accurate capture of the wake over potentially long times and/or distances; prime examples are the so-called blade-vortex interaction problem in rotorcraft aerodynamics or the exploitation of upstream vortices by a fish within a school or by birds/aircraft in formation flight.

This challenge of solving accurately and efficiently the flow from the device surface up to long distances downstream, and over long times, is the focal point of the approach proposed herein; so far in 2D. The Lagrangian vortex methods are quite appealing in this context. Indeed, these methods, which rely on a vorticity-based formulation, propose several computational assets that are particularly interesting for the wake regions. First, the very discretization

*Corresponding author:
Email address: philippe.billuart@uclouvain.be (P. Billuart).

of these methods can exploit the fact that the working variable, vorticity, is a compact quantity in wake flows, thus leading to a reduction in the number of degrees-of-freedom. Secondly, the formulation accommodates quite naturally the enforcement of the unbounded conditions of external flows. The Lagrangian discretization of vorticity into particles also allows to waive classical CFL conditions, thus allowing larger time steps. And finally, they entail very low dispersion and diffusion errors which puts them among the most efficient methods to accurately advect vortical structures over large distances [1, 2, 3, 4].

However, vortex methods are less suited to capture high Reynolds number boundary layers than classical Eulerian body-fitted grid solvers, e.g. finite difference, finite volume, finite element, etc, because the particles of a vortex method are almost always isotropic computational elements. This leads to a very large number of particles and thus a prohibitive computational costs to capture the near-wall gradients. This limitation can be mitigated by the use of Multi-Resolution methods or Adaptive Mesh Refinement (AMR) [5] even though this does not lift the isotropy constraint. This characteristic also implies that the body surface is usually treated as an immersed boundary where a non-trivial wall boundary condition which arises from the vorticity-based formulation must be applied. This is typically enforced using panel-based methods [6, 7, 8, 9], penalization methods [10, 11, 12, 13], or the more accurate immersed interface method [14]. Obtaining accurate wall quantities such as pressure and shear stress is also a challenge in such methods.

This naturally leads to the conclusion that one could exploit the advantages of Lagrangian vortex methods and body fitted-grid solvers in a coupled approach. The Eulerian solver is used to resolve the near-wall region, while the Lagrangian method handles the convection-dominated part of the flow, such as the wake. This coupling is based on a decomposition of the computational domain into two subdomains: one for the body-fitted solver and one for the vortex method. We can distinguish between two types of coupling: strong and weak couplings. In strong couplings [15, 16, 17], the overlapping of each subdomain can be partial and the Schwarz alternating method is then used to compute iteratively the boundary condition at each time step for each solver until reaching a desired level of consistency between them. Yet despite its good accuracy, Schwarz iterations are computationally prohibitive, especially in 3D, and require the same time step for both solvers. Weak coupling [18, 19, 20] does not perform iterations and the possible inconsistencies between the two subdomains must be controlled. However, this can allow the use of different time steps across the solvers. In such a coupling, the Lagrangian method solves the flow on the entire domain while the body-fitted Eulerian solver only solves the near-wall region in a much smaller domain. There is thus a full overlapping of the two subdomains which is limited to the near-wall region where the Lagrangian method is underresolved while the Eulerian grid can be much finer (see Fig 1). In these couplings, the Lagrangian method drives the Eulerian solver by imposing the boundary condition at the outer boundary of the near-wall domain whereas the Eulerian solution is used to correct the Lagrangian solution in the near-wall region. Since the coupling procedure is not iterated, the consistency between the two solutions is controlled via the information exchange methodology.

All the weak couplings developed until now [18, 19, 20] enforce velocity Dirichlet boundary conditions for the velocity at the outer boundary of the body-fitted solver domain. As these velocity values are obtained from the velocity field of the vortex method, any velocity mismatch between the solvers is translated into spurious vorticity that is then advected into the wake. These works also utilize a non-conservative scheme for the transfer of vorticity from the near-wall solver to the vortex method; i.e., the circulation is not conserved. Specifically, they rely on the interpolation of the vorticity field computed using the near-wall solver velocity field onto the particles inside the vortex method; the accuracy of this projection procedure greatly suffers in high vorticity gradient regions. All these works attempt to mitigate this circulation error by adding a vortex panel method on the body surface; Stock et al. [20] even elect to not correct the vortex particles located in the boundary layers. The recourse to a panel method, and to the involved circulation control, has however proven counterproductive as it leads to small oscillations in the velocity field. Indeed, since this field provides the boundary condition for the outer boundary of the body-fitted solver, it can generate spurious pressure oscillations in that solver. Those oscillations are even exacerbated by the distortion of the computational elements typical of Lagrangian vortex methods. Those two symptoms logically lead to noisy wall stresses that are unexploitable toward the computation of accurate aerodynamic forces.

We here propose novel approaches for the information exchanges between the Eulerian body-fitted solver and the Lagrangian vortex method, here a state-of-the-art Vortex Particle-Mesh (VPM) variant, to address the shortcomings identified above. Our coupling scheme uses a mixed boundary condition for the near-wall solver to properly match the vorticity fields of both solvers on the outer boundary and avoid the generation of spurious vorticity. In addition, our simple correction scheme of the VPM vorticity field by the near-wall Eulerian field guarantees a global conservation of the circulation: instead of interpolating the Eulerian vorticity on the VPM field, we interpolate the Eulerian velocity

and compute the corrected vorticity on the VPM grid. Thanks to this process, the local circulation is conserved within interpolation and discretization errors without requiring complex vorticity integration methods. Therefore, no additional wall treatment technique (panels, penalization or immersed interface methods) is used in the vortex method. To mitigate the pressure oscillations in the body-fitted solver due to the common flow distortion errors of the Lagrangian vortex methods, we propose to use two sets of particles, each redistributed at different time intervals. We also exploit the possibility offered by the weak coupling approach to advance the solvers with different time steps. Finally, contrary to previous contributions, we demonstrate the second order rate of convergence of our coupling scheme.

In Section 2, we present the two solvers used in our coupled method: the body-fitted Eulerian solver and the VPM method. Next, we present the coupling strategy in Section 3. In Section 4, we propose guidelines on how to determine the various parameters involved in this coupling. Afterwards, in Section 5, we start by numerically proving the second order rate of convergence for this coupling approach. Then, we demonstrate its correct performance on the benchmark of the impulsively started cylinder at $Re = 550$, 3000 and 9500, and on the shedding past a cylinder at $Re = 200$ and 550. Finally, in Section 7, as an example of application, we present the results for the flow past an impulsively-started airfoil at $Re = 5000$. A conclusion of the presented work and future perspectives are presented in Section 8.

2. Component solvers

The solvers of interest in this work are (1) a Finite Difference (FD) solver for the Near-Wall (NW) region and (2) a Vortex Particle-Mesh (VPM) method, a state-of-the-art variant of Lagrangian vortex methods, for the bulk flow. We first briefly present these two solvers in Sections 2.1 and 2.2, then detail the coupling methodology in Section 3. We will only deal with stationary bodies for the remainder of this paper but will nevertheless draw the reader's attention to the items necessary to an extension to moving/deforming geometries in the relevant parts of the algorithm.

2.1. The Near-Wall solver: body-fitted Finite-Differences

As Near-Wall (NW) solver, we use an in-house body fitted Finite Difference (FD) solver working in the velocity-pressure formulation and characterized by a classical fractional step method [21, 22, 23]. An explicit second-order adaptive Adams-Bashforth scheme is used for the advective term whereas the diffusive term is handled using an implicit Crank-Nicholson scheme, leading to the following set of semi-discrete equations

$$\frac{(\boldsymbol{u}^* - \boldsymbol{u}^n)}{\Delta t^+} = \left(1 + \frac{1}{2}\frac{\Delta t^+}{\Delta t^-}\right)\boldsymbol{H}_h^n - \frac{1}{2}\frac{\Delta t^+}{\Delta t^-}\boldsymbol{H}_h^{n-1} - \nabla_h \phi^n + \frac{1}{2}\nu\left(\nabla_h^2 \boldsymbol{u}^* + \nabla_h^2 \boldsymbol{u}^n\right) \tag{1}$$

$$\nabla_h^2 g = \frac{1}{\Delta t^+}\nabla_h \cdot \boldsymbol{u}^* \tag{2}$$

$$\frac{\left(\boldsymbol{u}^{n+1} - \boldsymbol{u}^*\right)}{\Delta t^+} = -\nabla_h g \tag{3}$$

$$\phi^{n+1} = \phi^n + g \tag{4}$$

$$P^{n+1} = \phi^{n+1} - \frac{\nu\,\Delta t^+}{2}\nabla_h^2 g \tag{5}$$

where Δt^+ and Δt^- are the current and previous time steps, respectively, $\boldsymbol{H}_h \triangleq (\boldsymbol{u}\cdot\nabla\boldsymbol{u})_h$ denotes the convective term, ν is the kinematic viscosity and P is the kinematic pressure (i.e., the pressure divided by the density). The equations above are ordered in the running order of the FD solver. A prediction for $\boldsymbol{u}^{n+1}$, $\boldsymbol{u}^*$, is first computed through Eq. (1). Next, a Poisson equation, Eq. (2), is solved. Finally, the predicted velocity is reprojected into a solenoidal field via Eq. (3), and the pressure field is obtained at the next time step via Eqs. (4) and (5). For the Poisson equation, a homogeneous Neumann boundary condition ($\frac{\partial g}{\partial \boldsymbol{n}} = 0$) is enforced; this is consistent with forcing the predictor normal velocity u_n^* to its exact value u_n^{n+1} on the FD solver boundaries. This system of equations thus requires the normal component velocity at time t^{n+1} to be known on all the boundaries. For the wall boundary, no-through flow and no-slip conditions are imposed. For the outer boundary, the boundary conditions are directly obtained from the vortex method (see discussion in Section 3.1).

In order to handle the near-wall regions, the solver uses structured orthogonal meshes with stretching. The spatial operators are written in the local orthogonal frame of each cell; this leads to a velocity field expressed in the local orthogonal components (tangential u_s and normal u_n components). The discretization also uses the staggered arrangement to avoid the spurious decoupling between the pressure and the velocity fields. Specificities regarding this solver are detailed in Appendix A.

The entire FD solver is parallelized using *OpenMP*, except for the Poisson equation (Eq. (2)) and the linear system resulting from the implicit treatment of diffusion; those are solved on a single CPU using the *PETSC* library [24, 25]. The Poisson equation is solved using a *LU* direct method while the implicit system is first prepared using a *Hypre BoomerAMG* preconditioner and next solved using the *GMRES* iterative method.

2.2. The Vortex Particle-Mesh method

The bulk flow solver used for this coupling is a Vortex Particle-Mesh (VPM) method. We here only provide a brief description; we refer to Cottet et al. [2], Winckelmans [1] and Chatelain et al. [26] for more thorough descriptions and discussions of the method. It relies on the vorticity-velocity ($\boldsymbol{\omega} - \boldsymbol{u}$) formulation of the Navier-Stokes equations for incompressible flows ($\nabla \cdot \boldsymbol{u} = 0$). For a planar 2D flow, the vorticity only has an out-of-plane component, $\boldsymbol{\omega} = \omega \boldsymbol{e}_z$; the equation to solve then reads

$$\frac{D\omega}{Dt} = \frac{\partial \omega}{\partial t} + \boldsymbol{u} \cdot \nabla \omega = \nu \nabla^2 \omega \tag{6}$$

where $\frac{D}{Dt}$ denotes the material derivative. Using a Helmholtz decomposition of the velocity field $\boldsymbol{u} = \boldsymbol{U}_\infty + \boldsymbol{u}_\omega$, we recover $\boldsymbol{u}_\omega$ by solving the following Poisson equation (also known as the Biot-Savart law)

$$\nabla^2 \boldsymbol{u}_\omega = -\nabla \times \omega \ . \tag{7}$$

The convective term is handled in a Lagrangian fashion: vorticity is discretized by means of particles, characterized by a position $\boldsymbol{x}_p$ and a strength (i.e., a circulation associated to the particle) $\alpha_p = \int_{S_p} \omega \, dS$ where S_p corresponds to the material surface associated to the particle. This discretization leads to two sets of ODEs integrated on the particles; one for their position, the other for their strength:

$$\frac{d\boldsymbol{x}_p}{dt} = \boldsymbol{u}(\boldsymbol{x}_p) \tag{8}$$

$$\frac{d\alpha_p}{dt} = \nu \int_{S_p} \nabla^2 \omega \, dS \ . \tag{9}$$

Both equations are advanced in time through a third order Runge-Kutta scheme with an adaptive time step.

As its name indicates, the VPM method also has an Eulerian component, which serves two purposes. One is the well-known problem of clustering and depletion of particles degrading the accuracy of vortex methods: a redistribution of the particle-carried vorticity onto the underlying mesh is performed at regular intervals, every N_r time steps, using an interpolation kernel, here the classical M'_4 scheme [27]. The second is computational efficiency. A grid-supported vorticity can be leveraged for computationally-intensive tasks [2], such as the evaluation of spatial differential operators and the solution of the Poisson problem of Eq. (7). The latter is performed by a Fourier-based solver which can enforce periodic, inflow/outflow or unbounded conditions [28, 29]; this solver is implemented using the open-source *FLUPS* library [30]. Moreover, we recall that the velocity and the differential operators are obtained on the grid while the ODEs are integrated on the particles. VPM methods thus need to interpolate information from the grid to the particles, and vice-versa. Those interpolations are readily performed using the same M'_4 interpolation scheme, as for the redistribution. For the remainder of this article, we will refer to the interpolation of fields from the mesh to the particles as *M2P* and, conversely, *P2M* for the interpolation from the particles to the mesh.

Finally, while a particle method is free of a classical CFL-like stability constraint, it still must satisfy a higher order criterion, Lagrangian in nature, to ensure the accuracy of the interpolation and quadrature operations inherent to the method [2]. This condition, based on the velocity gradient, translates the enforcement of non-crossing trajectories for the computational elements and enforces the accurate capture of their rotation with respect to each other

$$|\boldsymbol{S}|_{max} \, \Delta t < 0.2 \ldots 0.25; \quad |\omega|_{max} \, \Delta t < 0.2 \ldots 0.25 \tag{10}$$

where $\boldsymbol{S} \triangleq \frac{1}{2}\left(\nabla \boldsymbol{u} + (\nabla \boldsymbol{u})^T\right)$.

The entire solver is parallelized using the *TBB* and *OpenMP* libraries.

3. Coupling strategy

Our approach is based on that proposed by Daeninck et al. [18], which consists in overlapping computational subdomains. The Lagrangian domain, Ω_{VPM}, spans the whole domain of interest and it actually embeds the immersed body. The Eulerian domain, meanwhile, solely covers the near-wall region, Ω_{NW}. An example of such a domain decomposition is sketched in Fig. 1. The weak coupling approach [18] builds upon the following two premises:

- The VPM method solves the entire flow and enforces the far-field boundary conditions: unbounded, inflow-outflow or periodic. However, its solution is allowed to be under resolved in the near-wall region where very sharp features, such as boundary layers and separated shear layers, are present. Since those are properly resolved by the NW solver, which uses a body-fitted grid, the near-wall fields of the VPM method will be corrected using the NW solver solution.
- Conversely, the NW solver only solves the flow in the vicinity of the body and thus requires a boundary condition on its outer boundary, $\partial\Omega_{NW}$. This will be provided by the VPM solver, as it has the whole flow information at its disposal; i.e., the boundary layers, albeit at a coarse scale, the wake and the far-field boundary conditions.

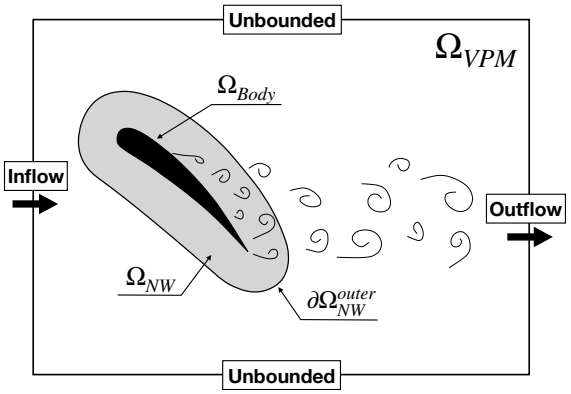


Fig. 1: Domain decomposition for the present coupling approach.

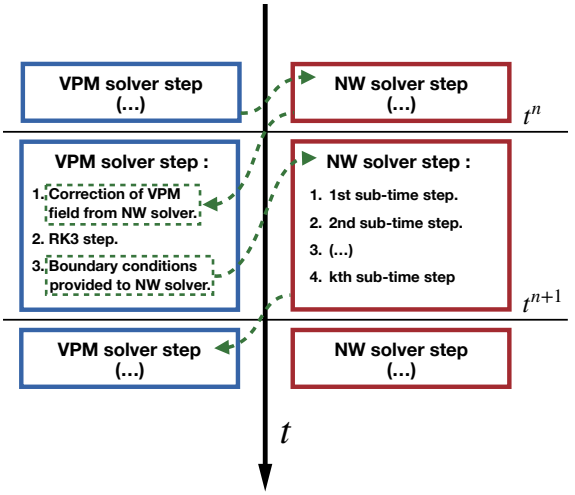


Fig. 2: Timeline execution of one VPM time step Δt_{VPM}. Dashed green arrows denote the transfer of information and the switch from one solver to another.

Practically, for each time step Δt_{VPM} of the VPM method, if we assume that all the fields in both solvers are known at time t^n, the weak coupling methodology brings those fields to time $t^{n+1} = t^n + \Delta t_{\mathrm{VPM}}$ in four steps:

1. The NW solver owns the more accurate velocity field $\mathbf{u}_{\mathrm{NW}}(\mathbf{x}, t^n)$ in the near-wall region. This field is leveraged to correct the vorticity field of the VPM solver, $\omega_{\mathrm{VPM}}(\mathbf{x}, t^n)$ in the part of the VPM domain that overlaps the NW domain.
2. The VPM solver integrates the vorticity evolution equation Eq. (6) over one time step Δt_{VPM}; the VPM velocity field $\mathbf{u}_{\mathrm{VPM}}(\mathbf{x}, t^{n+1})$ is then recovered through solving Eq. (7).
3. The outer velocity boundary conditions of the NW solver at time t^{n+1} are obtained using a spatial interpolation of the VPM velocity field.
4. Using the boundary condition obtained at Step 3, the NW solver advances its solution to t^{n+1} using one or several sub-time steps, Δt_{NW}.

The timeline of this execution is shown in Fig. 2.

Our approach distinguishes itself in the way the information is transferred between the two solvers, both for the NW outer boundary condition Step 3 (Section 3.1) and for the NW vorticity correction Step 1 (Section 3.3). In order to control pressure oscillations in the NW solver, two sets of particles with different redistribution frequencies are also introduced in the VPM solver (Section 3.2).

One could interpret the resulting complete solver as a VPM method where corrective terms are added in the near-wall region, with this correction including the call to the NW solver. This then naturally leads to the question whether the VPM solver should also include any enforcement of the immersed wall boundary conditions at all. In contrast to previous weak coupling techniques proposed so far [18, 19, 20], we here elect to not add any kind of wall treatment. This choice is discussed in Section 3.4.

Let us point out that the method naturally accommodates for different time steps in both solvers in order to capture the disparity of temporal scales encountered in aerodynamic external flows. This time step difference is even exacerbated by the respective numerical stability constraints of the two methods. The time step of the VPM solver is only constrained by a Lagrangian CFL, Eq. (10), which does not involve the mesh size but rather the intensity of the captured vorticity field. The time integration within the NW solver can involve constraints due to (1) stability, e.g. the classical CFL condition for explicit schemes or a condition on the diffusion stencil, and (2) accuracy in the case of implicit schemes.

Given its explicit component for advection and implicit treatment of diffusion, our FD solver will lead to potentially quite stringent CFL restrictions, especially at high Reynolds numbers. Therefore, Step 4 consists of multiple sub-time steps Δt_{NW}. This NW sub-time steps are still adaptive over the VPM time step $\Delta t_{\mathrm{VPM}} = \sum_{l=1}^{N_c} \Delta t_{\mathrm{NW}}^{l}$, with N_c the number of NW sub-time steps executed per VPM time step.

We note that the handling of a impulsive start requires the initialization of the NW solver fields as the corresponding potential flow (velocity and pressure fields). This is the only initialization as it will be translated next into the corresponding coarse boundary layers in the VPM solver through the correction step at the very start of the first VPM time step (see Fig 2).

3.1. Boundary conditions for the Near-Wall solver

The transfer of information from the VPM solver to the NW solver is achieved through the imposition of boundary conditions on the outer boundaries of the NW domain $\partial\Omega_{\mathrm{NW}}^{\mathrm{outer}}$. These boundary conditions only concern the velocity field as the pressure boundary conditions are implicitly enforced via the Neumann boundary condition from the Poisson equation (Eq. (2)).

Our approach uses boundary conditions that deviate from straightforward Dirichlet conditions on both velocity components as we aim to (1) ensure a continuity of vorticity and (2) conserve the flux of vorticity through the outer boundary of the NW solver. These two conditions will allow the irrotational character of the flow away from the separation zones to be preserved. Those two conditions are equivalent to imposing the velocity component normal to the boundary u_n and the vorticity ω, which can be in turn translated in mixed velocity conditions; i.e., Dirichlet and Neumann-type conditions for the normal and tangential components respectively. For $\mathbf{x}$ on $\partial\Omega_{NW}^{outer}$, we thus impose

$$u_n(\mathbf{x}) = \mathbf{u}_{\mathrm{VPM}}(\mathbf{x}) \cdot \hat{\boldsymbol{e}}_n(\mathbf{x}) \tag{11}$$

$$\frac{\partial}{\partial n}\left[h_s(\mathbf{x})\, u_s(\mathbf{x})\right] = \left[h_n(\mathbf{x})\, h_s(\mathbf{x})\right] \omega_{\mathrm{VPM}}(\mathbf{x}) + \frac{\partial}{\partial s}\left[h_n(\mathbf{x})\, u_n(\mathbf{x})\right] \ . \tag{12}$$

Those are formulated in an orthogonal coordinates system (n, s) following the directions normal and tangential to the boundary. It uses the classical definitions of metrics $h_n = \|\partial \boldsymbol{x}/\partial n\|$ and $h_s = \|\partial \boldsymbol{x}/\partial s\|$, and of the unit vectors $\hat{\boldsymbol{e}}_n = h_n^{-1}\partial \boldsymbol{x}/\partial n$ and $\hat{\boldsymbol{e}}_s = h_s^{-1}\partial \boldsymbol{x}/\partial s$.

Since different time steps are used in both solvers, the NW solver performs N_c adaptive sub-time steps to bring its solution to $t^{n+1} = t^n + \Delta t_{\mathrm{VPM}}$ and thus requires the outer velocity boundary condition at the intermediate sub-time steps $t^{n,m} = t^n + \sum_{l=1}^{m} \Delta t_{\mathrm{NW}}^{l}$ with $m = 1, \ldots N_c$ and $\Delta t_{\mathrm{NW}}^{l}$ the l-th NW sub-time step.

Let us now detail the enforcement of these boundary conditions in the case of the FD-based NW solver presented in Section 2.1. Specifically, the mesh-supported NW solver and VPM variables, depicted in Fig. 3, exchange information through the following operations:

1. At the end of the VPM time step, $t = t^{n+1}$, the velocity $\mathbf{u}$ and the vorticity ω are interpolated from the VPM mesh onto the outer boundary of the NW solver, $\partial\Omega_{\mathrm{NW}}^{\mathrm{outer}}$. This interpolation is performed using the same kernel as for the *M2P* interpolations of the VPM method, e.g. M_4'. The resulting boundary fields on $\partial\Omega_{\mathrm{NW}}^{\mathrm{outer}}$ are stored: the values at time t^n are still also available for temporal interpolation.

2. Next, at NW sub-time step m:

   2.1. We obtain the boundary values for $\mathbf{u}$ and ω at $t^{n,m}$ through linear interpolation in time from the values at t^n and t^{n+1}.

   2.2. We set the normal component to $u_n = \mathbf{u}_{\mathrm{VPM}} \cdot \hat{\boldsymbol{e}}_n$ to impose the Dirichlet condition of Eq. (11).

   2.3. The u_n values on $\partial\Omega_{\mathrm{NW}}^{\mathrm{outer}}$ are uniformly corrected to enforce the mass conservation in the NW domain. Here, in the case of non-deforming domain and body, the corrected u_n^c satisfies

$$\oint_{\partial\Omega_{\mathrm{NW}}^{\mathrm{outer}}} u_n^c \, dS = 0 \tag{13}$$

   where the integral is computed numerically, which actually constitutes a compatibility condition necessary to the convergence of the pressure Poisson solver (Eq. (2)).

   2.4. We impose the Neumann condition of Eq. (12) by means of ghost values u_s^{ghost} beyond the boundary of our staggered grid, see Fig. 3. Specifically, the ghost tangential velocities u_s^{ghost} are obtained by solving the centered second order finite difference discretization of Eq. (12) and injecting the values of u_n^c on the boundary edges, the interpolated vorticity ω_{VPM} at the boundary vertices, and the tangential velocities at the interior edge $u_s^{I-1/2,j}$. The final expression for u_s^{ghost} at index j is then

$$u_s^{\mathrm{ghost,j}} = \frac{1}{h_s^{I+1/2,j}} \left[\Delta n \left(h_n^{I,j} h_s^{I,j} \omega_{VPM}^{j} + \frac{\left(h_n^{I,j+1/2} u_n^{c,j+1/2} - h_n^{I,j-1/2} u_n^{c,j-1/2} \right)}{\Delta s} \right) + h_s^{I-1/2,j} u_s^{I-1/2,j} \right], \tag{14}$$

   where the couple (I, j) are indices covering all the vortex nodes along $\partial\Omega_{\mathrm{NW}}^{\mathrm{outer}}$. Index I refers to the largest vorticity nodes index in the $\hat{\boldsymbol{e}}_n$ direction, while j refers to the vorticity nodes index in the $\hat{\boldsymbol{e}}_s$ direction (having multiple values since varying along $\partial\Omega_{\mathrm{NW}}^{\mathrm{outer}}$). Δn and Δs are the uniform resolutions in the computational domain for the normal and tangential directions. It is important to note that, due to the implicit treatment of the diffusive term in Eq. (1), the interior tangential velocities $u_s^{I-1/2,j}$ are in reality unknowns, and therefore Eq. (14) is also handled in an implicit way; i.e., included into the linear system resulting from the implicit diffusion.

3.2. A spatially-varying redistribution frequency

In our presentation of the VPM method, we mentioned the importance of handling the Lagrangian distortion of the particles. Left unchecked, it ruins the accuracy and convergence of the method. A VPM simulation typically performs a redistribution of the particles every few time steps; it thus ensures that the resulting distortion remains acceptable all the while guaranteeing robustness and efficiency.

Yet, numerical experiments indicate that even an acceptable distortion leads to weak numerical noise in the interpolated fields, such as the velocity field sampled on the boundary $\partial\Omega_{\mathrm{NW}}^{\mathrm{outer}}$. While the VPM method is insensitive to such numerical fluctuations, these can be extremely detrimental when used as a boundary condition for a velocity-pressure formulation. Indeed, such spatio-temporal fluctuations in normal velocity will induce instantaneous changes in the pressure field, through the Eqs. (2) to (5). Numerical experiments (not presented for the sake of brevity) clearly demonstrate that these fluctuations are introduced at the redistribution frequency (every 3, 5 time steps) and render the wall-based measurements of aerodynamic forces unusable.

The same numerical experiments also show that a redistribution performed at every VPM time step makes this noise negligible. However, operating a particle-mesh method in such a way harms its accuracy in the advection of wake vortical structures. We reconcile these two computational objectives by proposing here a novel approach: a particle-mesh method with a spatially-varying redistribution frequency. While this approach is applicable to an arbitrary number of frequencies, we restrict our discussion to the case of two subsets of particles, each operating at its own redistribution frequency, as shown in Fig. 4:

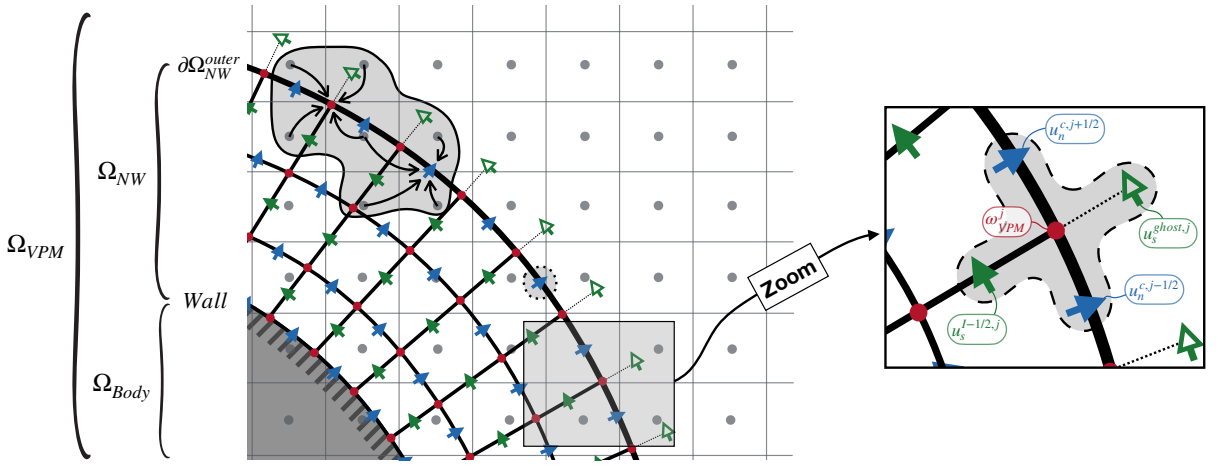


Fig. 3: Near-wall solver boundary condition enforcement: the NW solver staggered mesh is in the foreground with its variables u_s ( ), u_n ( ), ω ( ) and u_s^{ghost} ( ); the VPM mesh ( ) is in the background. Spatial $M2P$ M_4' interpolation (step 1 -). Correction of u_n to u_n^c (step 2.3 -). Ghost tangential velocity computation (step 2.4 - ( ) - presented on the zoom). N.B: for the sake of clarity, the represented interpolation stencil is narrower than the one actually used; i.e., M_4' (step 1).

- The first subset works at a unit redistribution frequency ($N_r = 1$) and occupies a small region of interest Ω_1, which for the coupling application encompasses the NW domain, Ω_{NW}; its particles have positions $\mathbf{x}_{p,1}$ and strengths $\alpha_{p,1}$.
- The second subset spans the whole domain, $\Omega_2 = \Omega_{\text{VPM}}$ and thus overlaps Ω_1. The particles in this set, described by $\mathbf{x}_{p,2}$ and $\alpha_{p,2}$, are redistributed every N_r steps.

In order to obtain the complete vorticity field on the mesh $\omega_{VPM,ij}$, we blend the two sets of particles using the indicator function $1^{\delta}_{\Omega_1}$ for Ω_1:

$$\omega_{VPM,ij} = 1^{\delta}_{\Omega_1}(\mathbf{x}_{ij})\, P2M(\mathbf{x}_{p,1}, \alpha_{p,1}) + \left(1 - 1^{\delta}_{\Omega_1}(\mathbf{x}_{ij})\right) P2M(\mathbf{x}_{p,2}, \alpha_{p,2})\ . \tag{15}$$

In order to ensure a consistent grid field, the indicator function $1^{\delta}_{\Omega_1}$ is mollified and truncated with respect to the support of the particles of subset 1: it has to transition smoothly from zero to one well within Ω_1, so that it is equal to zero outside Ω_1 but also equal to zero on the outer region of Ω_1. The transition is performed over a length δ represented by the dark gray region in Fig. 4. Specifically, this margin between the boundary of Ω_1 and the support of $1^{\delta}_{\Omega_1}$ has to account for the stencil width of M_4' and for the advection of particles into Ω_1. We note, additionally, that the transition of $1^{\delta}_{\Omega_1}$ should be some distance away from $\partial\Omega^{\text{outer}}_{\text{NW}}$ to preserve it from the numerical noise mentioned above.

Strictly speaking, the blending operation does not conserve circulation. This discrepancy should be easily controlled though, through the blending transition thickness, and should not affect spatial and temporal convergences. This is confirmed by the parametric study of Section 4: in practice, for a large enough transition, the associated errors are dominated by other discretization errors.

3.3. VPM vorticity correction

The correction of the vorticity field by information from the NW fields constitutes the sole vorticity generation mechanism as the VPM solver does not include any wall treatment. This procedure is performed on the mesh of the VPM solver through the following steps:

1. At $t = t^{n+1}$, after the N_c NW sub-time steps, the velocity $\mathbf{u}_{\text{NW}}$ is interpolated using third order Lagrange polynomials from the NW mesh onto the VPM grid but using a staggered velocity arrangement, as shown in Fig. 5; we denote this interpolated velocity field $\mathbf{u}_{\text{VPM,corr}}$. Additional details regarding this interpolation are provided in Appendix A.1.

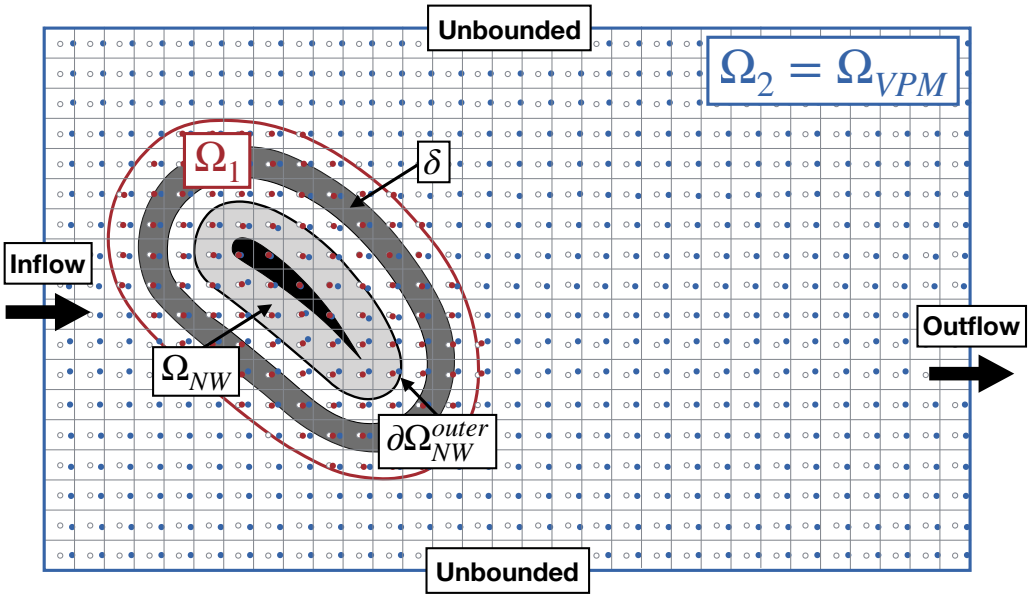


Fig. 4: Spatially-varying redistribution frequency: the subset of particles redistributed at every VPM time step ($N_r = 1$) is denoted by (●), while the other subset, redistributed every $N_r = 5$ step, is represented by (●). The VPM mesh is denoted by (○).

2. The velocity field $\mathbf{u}_{\text{VPM,corr}}$ inside the body is set to the body velocity (as obtained from its translation, rotation, or more complex deformations). In the present case of a stationary rigid object, it is simply extended as $\mathbf{u}_{\text{VPM,corr}} = \mathbf{0}$.

3. The vorticity $\omega_{\text{VPM,corr}}$ that corresponds to this corrected velocity field is computed as

$$\boldsymbol{\omega}_{\text{VPM,corr}} = \omega_{\text{VPM,corr}}\, \boldsymbol{e}_z = \nabla_h \times \mathbf{u}_{\text{VPM,corr}} \tag{16}$$

over the points of the overlapping region for which the stencil for the curl operator can be evaluated using corrected velocity only; let us denote it as $\Omega_{\text{NW}}^{corr}$. A staggered velocity interpolation grid has been preferred to a collocated one because (1) the curl stencil is then twice as compact, leading to a better circulation conservation within a VPM cell, and (2) the curl operator is then consistent with the four-point discretization of the integral of velocity on the VPM cell edges:

$$\alpha_{cell}^{i,j} \simeq h_{VPM}^2\, \omega_{\text{VPM,corr}}^{i,j} = \oint_h \mathbf{u}_{\text{VPM,corr}} \cdot d\boldsymbol{l} = h_{VPM}\, \left[\left(u_y^{i+1/2,j} - u_y^{i-1/2,j}\right) - \left(u_x^{i,j+1/2} - u_x^{i,j-1/2}\right)\right] , \tag{17}$$

where h_{VPM} is the VPM cell size and $\alpha_{cell}^{i,j}$ is the circulation within a specific cell (i, j).

4. This vorticity $\omega_{\text{VPM,corr}}$ is next integrated into the uncorrected grid vorticity

$$\omega_{\text{VPM}}(\mathbf{x}_{ij}, t^{n+1}) = 1_{\Omega_{\text{NW}}^{corr}}(\mathbf{x}_{ij})\, \omega_{\text{VPM,corr}}(\mathbf{x}_{ij}, t^{n+1}) + \left(1 - 1_{\Omega_{\text{NW}}^{corr}}(\mathbf{x}_{ij})\right)\, \omega_{\text{VPM}}(\mathbf{x}_{ij}, t^{n+1}) , \tag{18}$$

where $1_{\Omega_{\text{NW}}^{corr}}$ is the indicator function for the region $\Omega_{\text{NW}}^{corr}$.

As this procedure is performed at the beginning of the VPM time step, the subset of particles redistributed at every time step $(\mathbf{x}_{p,1}, \alpha_{p,1})$ immediately benefits from this correction. The other subset, $(\mathbf{x}_{p,2}, \alpha_{p,2})$, only obtains this information every N_r VPM time steps. This is of no consequence as the first subset prevails in the NW region, per the treatment described in Section 3.2. The VPM method thus has a corrected vorticity at the beginning of its time step and will obtain a Biot-Savart velocity field that includes this correction.

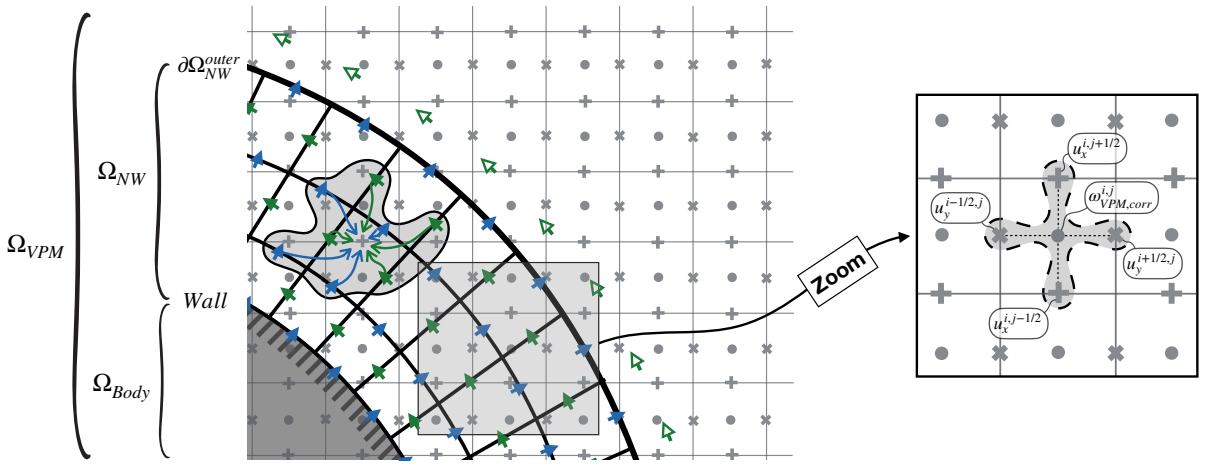


Fig. 5: VPM correction: the NW solver staggered mesh is in the foreground with its variables u_s ( ), u_n ( ), and u_s^{ghost} ( ); vorticity and velocity on the VPM mesh, ( ), and staggered interpolation grid (u_x: , u_y:) receiving the NW velocity are in the background. Spatial interpolation (step 1 -). Corrected vorticity computation (step 3 - - presented on the zoom). N.B: for the sake of clarity, the represented interpolation stencil is narrower than the one actually used; i.e., third order Lagrange interpolation (step 1).

3.4. Circulation conservation

In the weak couplings developed so far [18, 19, 20], the transfer of vorticity from the NW solver to the vortex method is non-conservative; i.e., the circulation is not conserved. Specifically, authors rely on the interpolation of the NW vorticity field onto the particles inside the vortex method; the accuracy of this projection procedure greatly suffers in high vorticity gradient regions because of sampling errors. This non-conservation of circulation forced those authors to complement the VPM solver with a wall enforcement scheme, either a panel method [7], a penalization technique [12], or a high order Immersed Interface Method [14]. The use of one of those techniques also permitted to enforce the no-through flow and no-slip conditions on the body surface within the VPM time step. However, the results have shown that those wall treatment techniques were counter-productive: a corrective step attempts to cancel the spurious slip and through-flow at the solid boundary but in a very under-resolved manner, a condition not too well tolerated by the three schemes mentioned above. Numerical experiments by Daeninck[1] have shown that this leads to large numerical oscillations in the near-wall vorticity, which in turn affects the velocity field evaluated on the outer boundary $\partial\Omega_{NW}^{outer}$ and then induces instantaneous changes in the NW pressure field, eventually leading to unusable wall-based measurements forces (see similar discussion in Section 3.2)

This shortcoming has motivated our use of a different correction step in order to avoid the need of an explicit wall enforcement technique. We show hereunder that the proposed correction of the near-wall vorticity field within VPM is sufficient for an efficient and robust coupling.

In order to conserve the circulation between the NW and the VPM solvers, one possibility is to compute, in the NW solver, the average vorticity over each VPM cell. This averaged vorticity is then transferred as $\omega_{\text{VPM,corr}}$ to the VPM solver. However, computing the exact averaged vorticity can be geometrically complex and expensive. If approximate quadrature rules are used, then the sampling errors are reduced but not eliminated.

Therefore, instead of transferring the vorticity directly from the NW solver to VPM, the present approach relies on the interpolation of the velocity from the NW solver to the VPM grid. And since the velocities are interpolated onto a staggered arrangement, the curl operator is fully consistent (Eq. (17)). This method provides an improved conservation of the circulation, albeit not exact, and at the cost of a simple pointwise interpolation. Indeed, the error on the circulation now consists in the error on any contour integral of the velocity transferred from the NW to the VPM solver, as clarified in the paragraphs hereunder.

When we consider a single VPM cell using the present scheme, the circulation is not exactly conserved because the vorticity in the cell is computed using only the 4 interpolated velocities, obtained as pointwise values. If the NW

[1] Private communication.

cell size is much smaller than the VPM cell size, then sampling errors can affect the accuracy of the approximated contour integral (and thus the computed value of vorticity) when large velocity gradients are present. Now, let us consider the following contour (see left part of Fig. 6): $\partial\Omega_{\mathrm{BL}}$ starts in the upper part or outside of the boundary layer, where the two mesh resolutions agree, it dives through the boundary layer, goes into the body, and comes out again and to close itself above the boundary layer after a few h_{VPM}'s. The sampled velocity above the boundary layer does not suffer from aliasing because the NW and VPM cell sizes are forced to match (see the parametric studies of Section 4) and is within $O\left(h_{VPM}^3\right)$ of the NW solver velocity. The velocity inside the body is null and the velocity on the segments crossing the boundary layer is dominated by components which are normal to the contour. The circulation about this contour can then be expected to be accurate. Finally, we can look at a contour near $\partial\Omega_{NW}^{outer}$ and encompassing the whole body (see right part of Fig. 6). Again, the sampling and interpolation errors on the velocity are small since the NW cell size is forced to match the VPM cell size on $\partial\Omega_{NW}^{outer}$. Therefore, the circulation computed as a contour integral of the interpolated velocities matches that of the same contour integral in the NW solver. And since the curl operator is consistent, the circulation computed as the integral of the correction vorticity in the VPM solver thus also matches the total circulation of the NW solver.

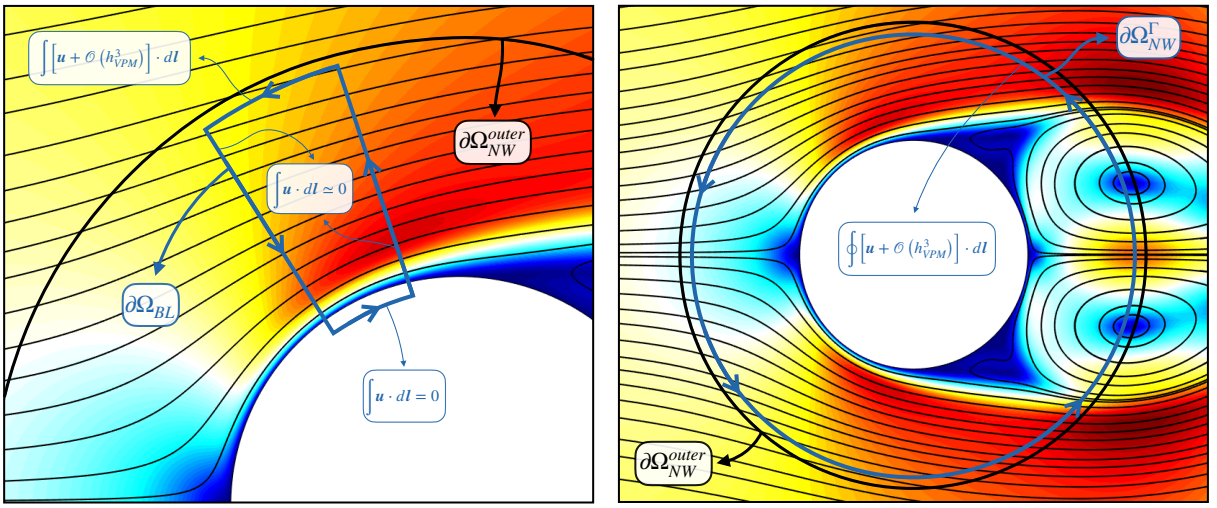


Fig. 6: Contours $\partial\Omega_{BL}$ and $\partial\Omega_{NW}^{\Gamma}$ designed to capture the boundary layer intensity (left) and the total circulation over the NW domain (right). For the sake of illustration, the streamlines and the norm of the velocity field from the impulsively starting cylinder test case at $Re = 550$ at $t^* \simeq 4$ are presented in the background (see Section 6.1).

The present scheme thus provides a very good conservation at scales corresponding to a few VPM cell sizes and of the global circulation around the body, despite not being exact locally. Furthermore, the numerical noise in the local circulation, is of little consequence. Indeed, the part of the flow resolved by the vortex code (and only the vortex code) is not influenced by the intricate details at the scales of the near-wall region, but only by scales a bit larger. Indeed, the first multipole moments of patches of the boundary layer would be accurately predicted by the vorticity transferred on the VPM mesh. Thanks to this large-scale conservation of circulation, the above correction enforces the no-slip and no-through flow conditions on the object at each VPM time step, and at the resolution of the VPM solver. This suffices for performing the next VPM time step. This vorticity correction procedure thus represents a very good trade-off between accuracy (good circulation conservation at the VPM scale) and computational cost (using only a number of pointwise interpolations equivalent to the number of vorticity points to correct).

These properties of the correction scheme lead to two important consequences: (1) the present coupling does not require the explicit control of circulation and (2) the computed VPM velocity field is sufficiently smooth and accurate in the vicinity of $\partial\Omega_{NW}^{outer}$ to provide the NW boundary condition there. The verification cases (Section 6) and the application (Section 7) should substantiate this claim of robustness.

4. Guidelines for the coupling parameters

The present coupling method involves several numerical and geometrical parameters whose effects on the coupling performance are discussed here. This discussion is based on extensive parametric studies. We only present here the conclusions of those studies in the form of guidelines.

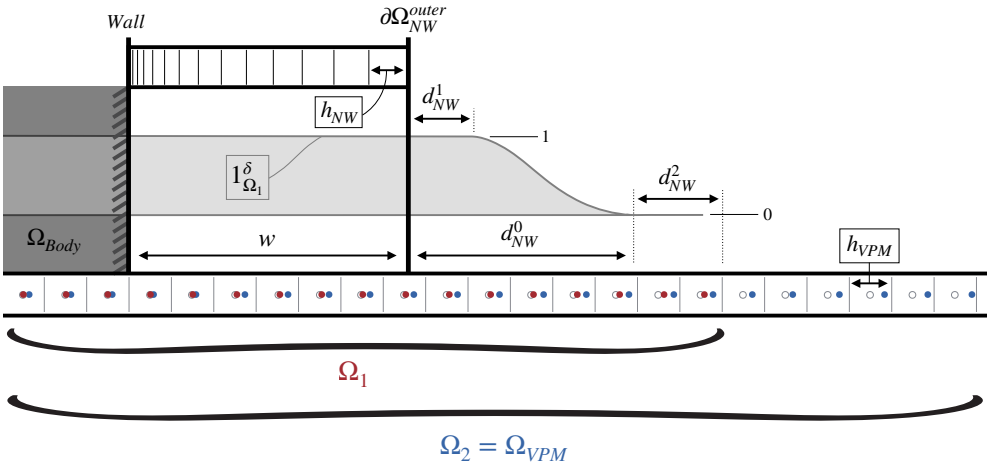


Fig. 7: Coupling parameters: the subset of particles redistributed at every VPM time step ($N_r = 1$) is denoted by (●), while the other subset, redistributed every $N_r = 5$ step, is represented by (●). The VPM mesh is denoted by (○)

The parameters involved are listed hereunder and presented in Fig. 7:

- w: the width of the NW domain.
- d^1_{NW}: the extent of the unit value of the mollified indicator function $1^{\delta}_{\Omega_1}$ beyond the NW outer boundary $\partial\Omega^{\text{outer}}_{\text{NW}}$;
- d^0_{NW}: the extent of the non-zero value of the mollified indicator function $1^{\delta}_{\Omega_1}$ beyond the NW outer boundary $\partial\Omega^{\text{outer}}_{\text{NW}}$; the width of the $1^{\delta}_{\Omega_1}$ transition is defined as $\delta \triangleq \left(d^0_{NW} - d^1_{NW}\right)$.
- d^2_{NW}: the margin between the boundary of Ω_1 and the support of $1^{\delta}_{\Omega_1}$.
- h_{VPM}: the spatial resolution of the VPM solver.
- h_{NW}: the spatial resolution of the NW grid at the outer boundary $\partial\Omega^{outer}_{NW}$.

Guidelines for h_{NW} and h_{VPM}: The resolution and stretching for the NW mesh (and h_{NW} by implication) shall be set in a way to capture the vortex structures everywhere in Ω_{NW}. Similarly, the uniform VPM spatial resolution h_{VPM} shall be set to capture the vortex structures in the non-overlapping flow domain only ($\Omega_{VPM}\backslash\Omega_{NW}$). Consequently, the cell size of the NW and VPM solvers at the outer boundary shall match: $h_{NW} = h_{VPM}$. With respect to the recommended situation above, refining the NW mesh while keeping h_{VPM} constant (or experimenting the opposite) will not benefit the global accuracy, which is limited by the coarsest resolution among both solvers on $\partial\Omega^{outer}_{NW}$. In addition, a local refinement of the VPM mesh in the NW region using a multi-resolution solver, while still complying with our recommendations above, will efficiently improve the global accuracy. Indeed, a better capture of the under-resolved VPM vortical structures in Ω_{NW} will radiate an enhanced boundary condition to the NW solver.

Guideline for w: The quantity of interest for the NW domain width is actually the ratio w/h_{VPM}. First, we recall that the most under-resolved VPM vortical structures are those at the wall and induce small errors in the velocities evaluated at the boundary $\partial\Omega^{\text{outer}}_{\text{NW}}$. A larger value for w/h_{VPM} will then lead to a more accurate boundary conditions for the NW solver. But a larger value for w/h_{VPM} also leads to (1) more computational elements for the NW solver and (2) a larger area of the computational domain solved in an Eulerian manner, thus affecting the performance of the combined solver for the advection of vortical structures in the NW region. When working with a uniform VPM

resolution, one must then achieve a trade-off. The NW domain width should be set to a fraction of the characteristic size of the object: $w = 0.5\text{-}1.5\ L_c$. Such a width, together with the recommendations mentioned above for h_{NW} and h_{VPM}, will naturally lead to a close-to-optimal w/h_{VPM} value. In contrast, if a multi-resolution VPM solver is available, no trade-off is required. Indeed, a local refinement of the under-resolved structures in the NW region enables the same level of accuracy on $\partial\Omega_{\mathrm{NW}}^{\mathrm{outer}}$ when one reduces w and keeps coarse cells in the wake. Again, we note here the major interest of using a multi-resolution VPM solver.

Guideline for function $1^{\delta}_{\Omega_1}$: The values chosen for those two parameters result from tackling three constraints and numerical behaviors:

1. Too small a transition width δ (with respect to the mesh size h_{VPM}) for $1^{\delta}_{\Omega_1}$ affects the conservation of circulation during the blending operation of (15).
2. A large extent for the support of $1^{\delta}_{\Omega_1}$ essentially cancels the Lagrangian character of the VPM method and therefore degrades its performance for the advection of vortical structures from the NW region.
3. The use of two sets of particles reduces drastically the oscillations in the wall-based measurement of the aerodynamic forces. In spite of this, very small high frequency numerical noise subsists. The parametric study has shown that the amplitude of these oscillations decreases slightly with larger δ or d^1_{NW} and indicates that a distance $d^1_{NW} > 0$ is necessary.

In light of these three effects, the following trade-off has been set for the simulations performed in the Sections 6 and 7: $d^1_{NW} = 4\,h_{VPM}$ and $\delta \triangleq \left(d^0_{NW} - d^1_{NW}\right) = 8\,h_{VPM}$.

Finally, the Eulerian definition of Ω_{NW}, Ω_1 and $1^{\delta}_{\Omega_1}$ leads to two important CFL-like constraints on the handling of the two sets of particles in the coupled solver.

(1) As already mentioned in Section 3.2, the margin d^2_{NW} between the boundary of Ω_1 and the support of $1^{\delta}_{\Omega_1}$ has to account for the stencil width of M'_4 and for the advection of particles into Ω_1. Indeed, when the velocity is oriented towards the body, the inward displacement of the particles of subset 1 must be limited to avoid particle depletion in the support of $1^{\delta}_{\Omega_1}$. If we define u^2_{max} as the maximal velocity magnitude in the region covered by d^2_{NW}, this issue translates into the following constraint over d^2_{NW} :

$$d^2_{NW} > \Delta t_{VPM}\ u^2_{max} + \frac{1}{2}\ w_{M'_4}\ h_{VPM} \tag{19}$$

where $w_{M'_4} \triangleq 4$ is the stencil size of the M'_4 scheme. A non-compliance with this constraint can cause a significant loss of circulation.

(2) Conversely, the outward displacement of the particles should be limited to avoid that particles of subset 2 originating from Ω_{NW} reach the support of $(1-1^{\delta}_{\Omega_1})$ before being redistributed. Otherwise, this would translate in a slight degradation of the vorticity beyond d^1_{NW} because such particles would have missed some NW corrections during their N_r-time step lifetime. If we define u^1_{max} as the maximal velocity magnitude in the region covered by d^1_{NW}, this issue translates into the following time step constraint:

$$\Delta t_{VPM} < \frac{d^1_{NW} - \frac{1}{2}\ w_{M'_4}\ h_{VPM}}{N_r\ u^1_{max}}. \tag{20}$$

A non-compliance with this condition could result in a loss of accuracy of the method.

5. Convergence studies

In this section, we use the case of the hollow diffusing Gaussian vortex to study the global convergence rates. This case was also used by Gillis et al. [14] to conduct their own convergence studies. We perform this study for each solver individually and for their combination, once coupled. The vortex is centered at $\mathbf{x}_c = \mathbf{x}^i_c$, the center of the inner boundary from the NW solver (see Fig. 8), and is characterized by the following analytical vorticity, ω^G, and velocity, $\boldsymbol{u}^G = (u^G, v^G)$, fields:

$$\omega^G(x,y,t) = \frac{\Gamma}{\pi}\frac{1}{(\sigma^2 + 4\nu t)}\exp\left(-\frac{|\mathbf{x} - \mathbf{x}_c|^2}{\sigma^2 + 4\nu t}\right), \tag{21}$$

$$\mathbf{u}^G(x,y,t) = \frac{1}{2\pi}\frac{\Gamma \boldsymbol{e}_z \times (\mathbf{x}-\mathbf{x}_c)}{|\mathbf{x}-\mathbf{x}_c|^2}\left[1-\exp\left(-\frac{|\mathbf{x}-\mathbf{x}_c|^2}{\sigma^2+4\nu t}\right)\right] . \tag{22}$$

The core radius, σ, is set to $2D$ where $D = 2R = D_i$ is the diameter of the inner circle boundary from the NW solver (see Fig. 8). We consider this problem at a Reynolds number $Re \triangleq \frac{1}{\pi}\frac{\Gamma}{\nu} = 1000$ and evaluate the errors at a dimensionless time $t^* \triangleq t\Gamma/R^2 = 32$. This time, together with the eccentric domain discussed below, allows the advection of vorticity both into and from the NW domain.

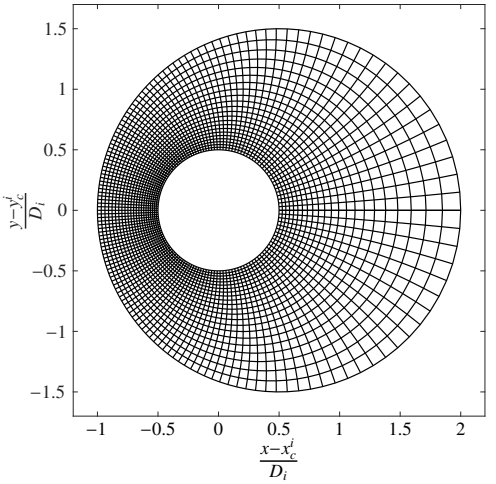


Fig. 8: NW solver mesh used for the convergence study.

We study the convergence of the 2- and ∞-norms of the errors on the velocity and vorticity fields for both solvers, and on the pressure field for the NW solver. Taking the analytical field as reference, we define the following dimensionless errors

$$\begin{aligned}
E_2^{\mathbf{u}} &= \frac{1}{\Gamma}\sqrt{\sum_{i,j}|u_{ij}-u_{ij}^G|^2\,\Delta S^u_{ij} + \sum_{k,l}|v_{kl}-v_{kl}^G|^2\,\Delta S^v_{kl}} & E_\infty^{\boldsymbol{u}} &= \frac{R}{\Gamma}\left[\max_{i,j}|u_{ij}-u_{ij}^G| + \max_{k,l}|v_{kl}-v_{kl}^G|\right] \\
E_2^{\omega} &= \frac{R}{\Gamma}\sqrt{\sum_{i,j}|\omega_{ij}-\omega_{ij}^G|^2\,\Delta S_{ij}} & E_\infty^{\omega} &= \frac{R^2}{\Gamma}\max_{i,j}|\omega_{ij}-\omega_{ij}^G| \\
E_2^{P} &= \frac{R}{\Gamma^2}\sqrt{\sum_{i,j}|P_{ij}-P_{ij}^G|^2\,\Delta S_{ij}} & E_\infty^{P} &= \frac{R^2}{\Gamma^2}\max_{i,j}|P_{ij}-P_{ij}^G|
\end{aligned} \tag{23}$$

The expressions for the velocity and vorticity errors are valid for the NW and VPM methods. They are expressed with distinct surface elements ΔS^u_{ij} and ΔS^v_{kl} for the velocity components to reflect the fact that these errors are computed on a staggered grid for the NW solver. Considering two successive resolutions, (h_k) and (h_{k+1}), and their associated errors, we compute the convergence rates, r_2 and r_∞, as

$$r_2 = \frac{\log\left[E_2^k/E_2^{k+1}\right]}{\log\left[h_k/h_{k+1}\right]} \text{ and } r_\infty = \frac{\log\left[E_\infty^k/E_\infty^{k+1}\right]}{\log\left[h_k/h_{k+1}\right]} . \tag{24}$$

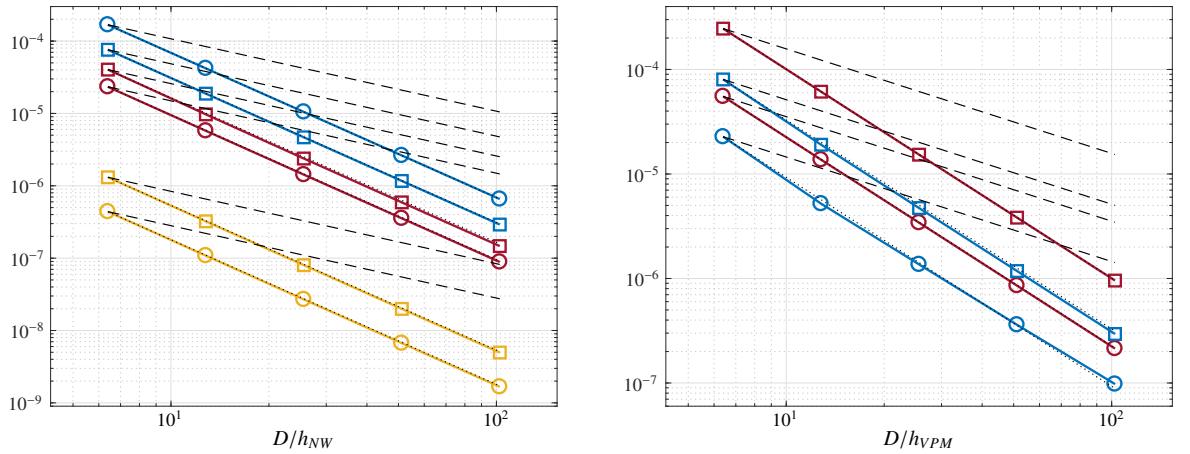
NW solver

For this convergence study, the FD solver is run alone on a hollow domain with boundary conditions similar to those of the coupling approach (Section 3.1). Both components of the analytical velocity are enforced at the inner boundary, while the analytical normal velocity and vorticity are prescribed on the outer boundary.

This case is run on a cylindrical mesh deformed by means of a conformal transform that preserves the orthogonal property; this causes a flow through the outer boundary $\partial\Omega_{\mathrm{NW}}^{\mathrm{outer}}$ (see Fig. 8) which is a circle of diameter D_o and

centered at x_c^o. The eccentricity $|\boldsymbol{x}_c^o - \boldsymbol{x}_c^i|/D_i$ is set to 0.5 and the outer diameter is three times larger than the inner one, $D_o/D_i = 3$. For more details about the mesh and the conformal transform, we refer to Appendix B. This setup results in a non-axi-symmetric problem and utilizes the mixed boundary condition on the outer boundary in a non-trivial way, as the vortex lies at the center of the inner boundary.

This is a global convergence study: the maximal CFL number is kept constant at about 0.1. The time and spatial resolutions are thus decreased by the same factor along the convergence path. The results, presented in Fig. 9a and in Table B.6 (in Appendix B), exhibit second order convergence for the 2- and ∞-norms as expected. Those rates are consistent with the second order temporal and spatial schemes used for the NW solver.



(a) NW solver

(b) VPM solver

Fig. 9: Global convergence for individual solvers: $E_2^{\boldsymbol{u}}$( ), $E_\infty^{\boldsymbol{u}}$( ), E_2^{ω}( ), E_∞^{ω}( ), E_2^{P}( ), E_∞^{P}( ), $O(h)$ (- - -) and $O(h^2)$ (····).

VPM solver

The global convergence of the VPM method is studied on a square computational domain $[-20\,D; 20\,D]^2$ with the Gaussian vortex positioned in the center. Unbounded conditions are applied on the four edges of the box.

These VPM simulations are run at a constant maximal CFL number of about 0.26; all the particles are redistributed every five time steps. The results, presented in Fig. 9b and in Table B.7, exhibit mainly second order convergence for the 2- and ∞-norms, as expected. This rate agrees with the lowest order of accuracy of the spatial and temporal schemes, which are respectively second and third order accurate.

Coupling

The computational domains and parameters used above for the NW and VPM solvers are combined into the configuration for the coupled simulations of the diffusing vortex. The resulting setup appropriately stresses several aspects of the coupling: a ten-fold factor between the NW and VPM time steps, the spatially-varying redistribution frequency– $N_r = 1$ and 5– within VPM, a varying ratio between the NW and VPM mesh resolutions on $\partial\Omega_{\text{NW}}^{\text{outer}}$: $h_{\text{NW}}/h_{\text{VPM}} \simeq 1$ on the right of Fig. 8 and $h_{\text{NW}}/h_{\text{VPM}} \simeq 0.2$ on the left.

The error computations for the NW and VPM solvers account for the roles of the respective solvers: as the NW solver provides the most accurate solution over Ω_{NW}, the VPM error is here only computed on the region $\Omega_{\text{VPM}} \setminus \Omega_{\text{NW}}$. The results, presented in Fig. 10 and in Tables B.8 and B.9, indicate that the coupling achieves a second order convergence. As the individual solvers are both second order accurate, this demonstrates that all the operations involved in the coupling maintain this order: the spatial interpolation of information between the NW and VPM solvers in both directions (Section 3.1 and 3.3), the linear interpolation in time for the NW boundary conditions, and the weak coupling strategy itself.

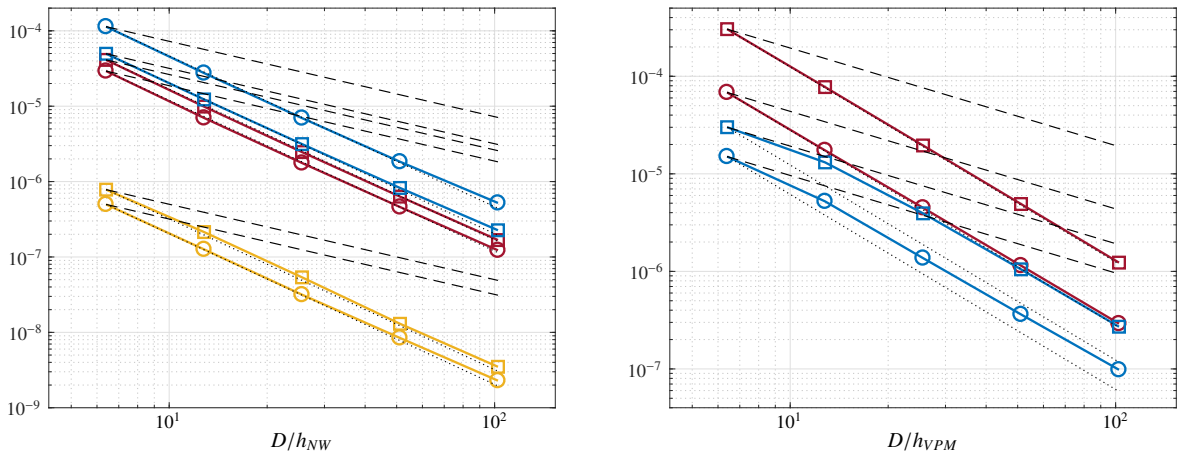


Fig. 10: Global convergence for the coupling in the NW domain (left) and VPM-only domain (right). $E_2^{\boldsymbol{u}}$( ), $E_\infty^{\boldsymbol{u}}$( ), E_2^{ω}( ), E_∞^{ω}( ), E_2^{P}( ), E_∞^{P}( ), $O(h)$ (- - -) and $O(h^2)$ (····).

6. Verification: the flow past a cylinder

We now verify the proposed coupling on the benchmark problem of the flow past a cylinder of diameter $D = 2R$ and at various Reynolds numbers $Re = (U_\infty D)/\nu$, both at the impulsive start and in the shedding regime. In particular, we examine the consistency of the forces captured by the two constituent methods, verify them against competing approaches, and assess the performance at capturing wall vorticity.

We first recall that the forces on the immersed body can be estimated from either the NW or the VPM solver. In the NW solver, they are computed by integrating the shear and pressure stresses around the body surface. In the VPM solver, we use a control volume approach initially proposed by Noca et al. [31], and specifically, the flux-based expression. For a stationary and non-deforming body, it simplifies to

$$\frac{\boldsymbol{F}}{\rho} = \oint_{\partial\Omega_c} \hat{\boldsymbol{n}} \cdot \boldsymbol{\gamma}_{\text{flux}}\, dS \tag{25}$$

where Ω_c is the control volume encompassing the body and $\hat{\boldsymbol{n}}$ is the normal unit vector to $\partial\Omega_c$. The flux $\boldsymbol{\gamma}_{\text{flux}}$ is given by

$$\begin{aligned}\boldsymbol{\gamma}_{\text{flux}} = \frac{1}{2}|\boldsymbol{u}|^2\boldsymbol{I} - \boldsymbol{u}\boldsymbol{u} - \frac{1}{\mathcal{N}-1}\boldsymbol{u}(\boldsymbol{x}\times\boldsymbol{\omega}) + \frac{1}{\mathcal{N}-1}\boldsymbol{\omega}(\boldsymbol{x}\times\boldsymbol{u}) \\ - \frac{1}{\mathcal{N}-1}\left[\left(\boldsymbol{x}\cdot\frac{\partial\boldsymbol{u}}{\partial t}\right)\boldsymbol{I} - \boldsymbol{x}\frac{\partial\boldsymbol{u}}{\partial t} + (\mathcal{N}-1)\frac{\partial\boldsymbol{u}}{\partial t}\boldsymbol{x}\right] \\ + \frac{1}{\mathcal{N}-1}\left[\boldsymbol{x}\cdot(\nabla\cdot\boldsymbol{T})\,\boldsymbol{I} - \boldsymbol{x}(\nabla\cdot\boldsymbol{T})\right] + \boldsymbol{T}\end{aligned} \tag{26}$$

in which $\mathcal{N}$ is the spatial dimension (2 for this paper), $\boldsymbol{I}$ is the identity tensor and $\boldsymbol{T} = \nu\left[\nabla\boldsymbol{u} + (\nabla\boldsymbol{u})^T\right]$ is the viscous stress tensor for an incompressible flow. The motivation for this approach is two-fold: (1) these formulas by Noca et al. do not involve the pressure field, making them quite attractive for vorticity-velocity formulations such as the VPM method; (2) this specific flux-based variant does not involve volume integrals over Ω_c and thus avoids the integration of under-resolved velocity and vorticity fields in the near-wall region, which would have inevitably led to noisy and inaccurate force estimations. An additional precaution is nonetheless taken for this surface integral. The under-resolved vorticity in the near-wall region can affect velocities some distance away from the wall through the Biot-Savart law; we thus use control volume surfaces $\partial\Omega_c$ that lie at or further than $\partial\Omega_{\text{NW}}^{\text{outer}}$ from the wall. Ultimately, let us make clear that the present exercise aims at a numerical verification: these VPM forces should not supplant the NW-based ones in applications as the latter are based on the finest mesh.

The remainder of this discussion relies on the following dimensionless quantities

$$t^* \triangleq \frac{t\,U_\infty}{D},\quad C_d \triangleq \frac{F_x}{\frac{1}{2}\rho\,U_\infty^2\,D},\quad C_l \triangleq \frac{F_y}{\frac{1}{2}\rho\,U_\infty^2\,D},\quad \omega^* \triangleq \frac{\omega\,D}{U_\infty},\quad P^* \triangleq \frac{P}{\frac{1}{2}U_\infty^2},\quad \text{and}\quad h^+ \triangleq \frac{h_{\mathrm{NW}}^{n,\mathrm{wall}}\,u_\tau}{\nu} \tag{27}$$

where $u_\tau^2 \triangleq |\tau_{\mathrm{wall}}|/\rho$ with τ_{wall} the shear stress at the wall, and $h_{\mathrm{NW}}^{n,\mathrm{wall}}$ the cell size in the wall-normal direction at the body surface in the NW solver.

6.1. Impulsive start

The NW mesh is polar with a stretching in the normal direction, as shown in Fig. 11. This stretching accommodates two requirements: (1) capturing the smallest structures in its own domain and (2) matching the NW and VPM resolutions on the outer boundary $\partial\Omega_{\mathrm{NW}}^{\mathrm{outer}}$. We note that a special attention was given to the normal size of the first cell $h_{\mathrm{NW}}^{n,\mathrm{wall}}$ that is such that $h^+ < 1$ for $t^* > 0.03$. This study considers the impulsive start at several Reynolds numbers; the corresponding spatial and temporal parameters are summarized in Table 1. For all simulations, the particle subset working at $N_r = 1$ and the corresponding indicator function $1_{\Omega_1}^{\delta}$ are set up following the conclusions of the parametric study of Section 4. The second particle subset operates at a redistribution frequency $N_r = 5$ for all cases.

Table 1: Mesh parameters and ratio of temporal resolution between both solvers for the impulsively started cylinder cases.

Re	w/R	R/h_{VPM}	$R/h_{\mathrm{NW}}^{n,\mathrm{wall}}$	$h_{VPM}/h_{\mathrm{NW}}^{n,\mathrm{wall}}$	$h_{\mathrm{NW}}^{\theta,\mathrm{wall}}/h_{\mathrm{NW}}^{n,\mathrm{wall}}$	$\Delta t_{\mathrm{VPM}}/\Delta t_{\mathrm{NW}}$ (min..**avg**..max)
550	1	18.3	178.5	9.8	4.7	1..**2**..2
3000	1	36.6	714.3	19.5	9.3	1..**2**..3
9500	1	146.3	2000	13.7	6.8	1..**4**..6

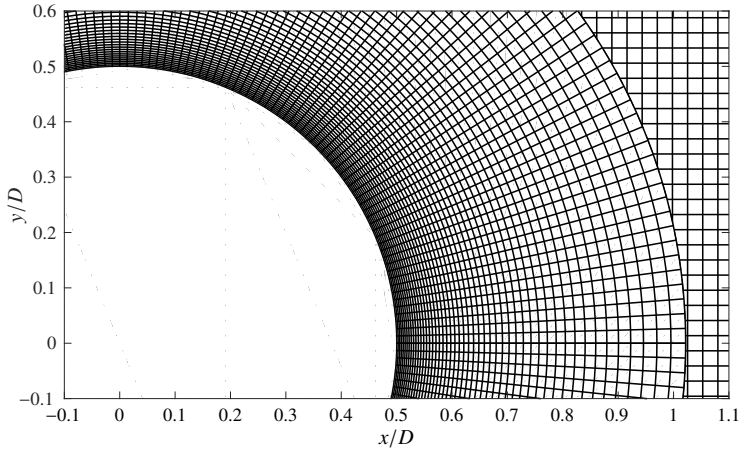


Fig. 11: Mesh used for the $Re = 550$ impulsively started cylinder test case. The VPM mesh is at the background and NW mesh is at the foreground.

$Re = 550$

A close inspection of the vorticity field shown in Fig. 12 reveals the excellent continuity of this field across the outer NW solver boundary. This consistency, in particular, confirms the effectiveness of the mixed velocity-vorticity boundary condition and of the vorticity correction step.

The simulation is performed up to $t^* = 10$. As the flow remains up/down symmetric for the short times considered in this benchmark, we only present the history of the drag coefficient in Fig. 13, according to the NW and VPM solvers. The flux formula used by the VPM solver is evaluated on a control surface situated at 1 D from the center of the cylinder. The agreement is excellent, between each other, and also with Gillis et al. [14] and Koumoutsakos and

Leonard [32] who both also used vortex methods. A zoom on the early times (until $t^* = 0.1$) is also presented and shows the good agreement with a theoretical expansion [33], valid only for short times,

$$C_d = \frac{\pi}{\sqrt{(Re\, t^*)}}\left[\left(2.257 + k - 0.141\,k^2 + 0.031\,k^3\right) + \left(8.996 - 41\,k + 143.8\,k^2 + 45.4\,k^3\right)t^{*2} + \left(20.848 - 314.08\,k - 1851.36\,k^2 - 194.8\,k^3\right)t^{*4} + \left(28.864 + 6.272\,k\right)t^{*6} + O\left(t^{*8}\right)\right] \tag{28}$$

where $k \triangleq 4\sqrt{t^*/Re}$. This expression stems from the temporal power series of the early boundary layer development. Its range of validity and convergence is not precisely known, but, logically, it increases with the Reynolds number.

The capture of the initial $t^{-1/2}$ decrease is challenging for any method but the present coupling handles it very well. We indeed observe an oscillation into the NW-based force curve but it quickly recovers to the correct trend. In Fig. 14, we compare the wall vorticity obtained by the NW solver with the one predicted by the above-mentioned works. Of note, the results of the present coupling are free of spurious oscillations, a feat enabled by the body-fitted NW solver. Such a smooth curve for ω^*_{wall} can only be produced at very fine resolutions in vortex methods that rely on the penalization [12] or immersed interface [14] techniques. For both times considered, the present coupling is in excellent agreement with the results of Gillis et al. [14], but for the first peak around $\theta = 0.3\,\pi$, the location of the maximum vorticity flux. The otherwise perfect agreement, and the fact that the wall-normal resolution of the NW mesh, $h^{n,\text{wall}}_{\text{NW}}$, is about twice as fine as that of [14] at the wall indicate that this localized difference could come from the treatment of the vorticity flux, which differs intrinsically between the approaches. Let us note, finally, that the VPM mesh in this coupling has a resolution h_{VPM} 5.6 times coarser than that of Gillis et al. [14].

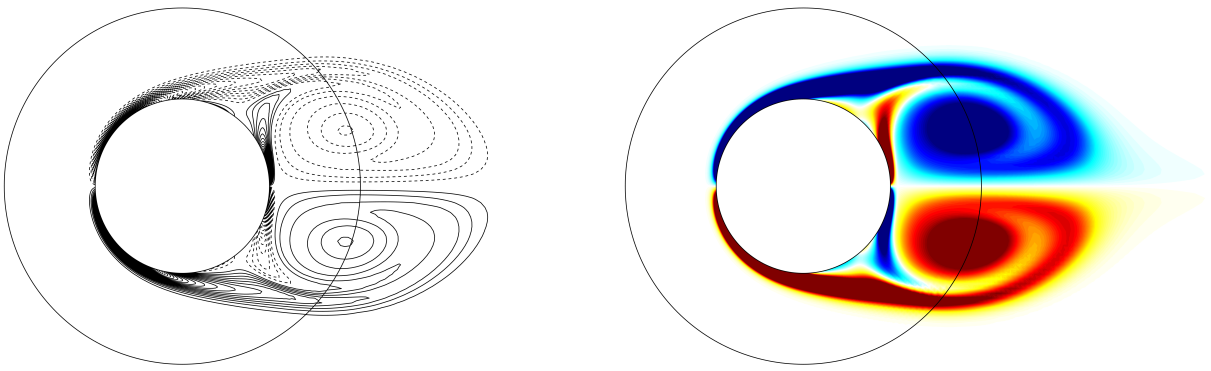


Fig. 12: Impulsively-started cylinder at $Re = 550$: contours of dimensionless vorticity at $t^* \simeq 4$ in the NW and VPM solvers. Contour levels are by steps of 1.5. The color plot is saturated for $|\omega^*| > 6$. The limit $\partial\Omega^{\text{outer}}_{\text{NW}}$ between the NW and VPM results is represented by a thin black line.

$Re = 3000$

The visualizations of this flow at $Re = 3000$ in Fig. 15 highlight an important feat of the coupling: the handling of fine vortical structures advected between the NW and VPM domains. Figure 16 shows the drag coefficient up to $t^* = 6$, with a zoom for the early times until $t^* = 0.06$. Up to $t^* \simeq 2$, the NW and VPM-based forces agree perfectly; past that point, one can observe oscillations in the VPM-based estimation. The time $t^* = 2$ corresponds to the advection of the first vortical structures into the region $\Omega_{\text{VPM}} \setminus \Omega_{\text{NW}}$; those structures are quite fine at such early times and, together with the relatively coarse VPM mesh resolution, could explain the marked oscillations between $t^* = 2$ and 3. At later times, the advected shear layers are thicker (see e.g. Fig. 15) and lead to weaker oscillations. This time $t^* = 2$ also marks the onset of a slight departure with respect to the references. The present VPM resolution, again 5.6 times coarser than that of Gillis et al. [14], probably leads to a slightly less accurate resolution of the wake dynamics and therefore to differences in the pressure at the wall. At the wall, the $h^{n,\text{wall}}_{\text{NW}}$ of the present approach is 3.5 times finer than Gillis et al. [14]. The wall vorticity is presented in Fig. 17 and leads to similar observations as for $Re = 550$.

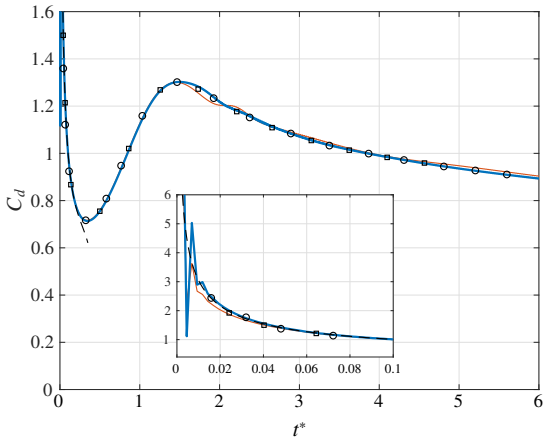


Fig. 13: Impulsively-started cylinder at $Re = 550$: Drag coefficient. Present coupling: evaluation by the FD solver (—) and by Noca formula on a control surface situated at 1 D from the center of the cylinder (—). Gillis et al. [14] (○). Koumoutsakos and Leonard [32] (□). Theoretical curve [33] (– –).

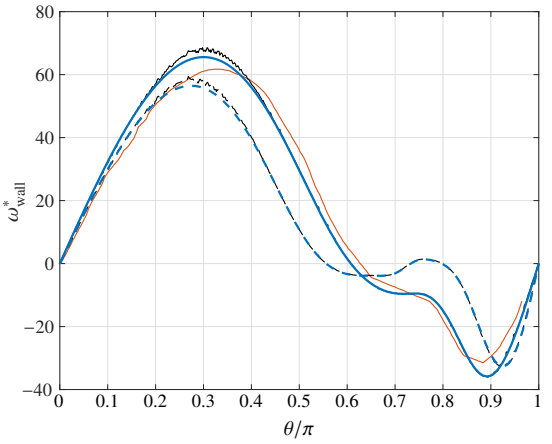


Fig. 14: Impulsively-started cylinder at $Re = 550$: wall vorticity ω^*_{wall} vs the azimuthal position θ ($\theta = 0$ at the stagnation point). Present coupling ($t^* = 1$: —, $t^* = 3$: – –), Gillis et al. [14] ($t^* = 1$: —, $t^* = 3$: – –) and Koumoutsakos and Leonard [32] ($t^* = 1$: —).

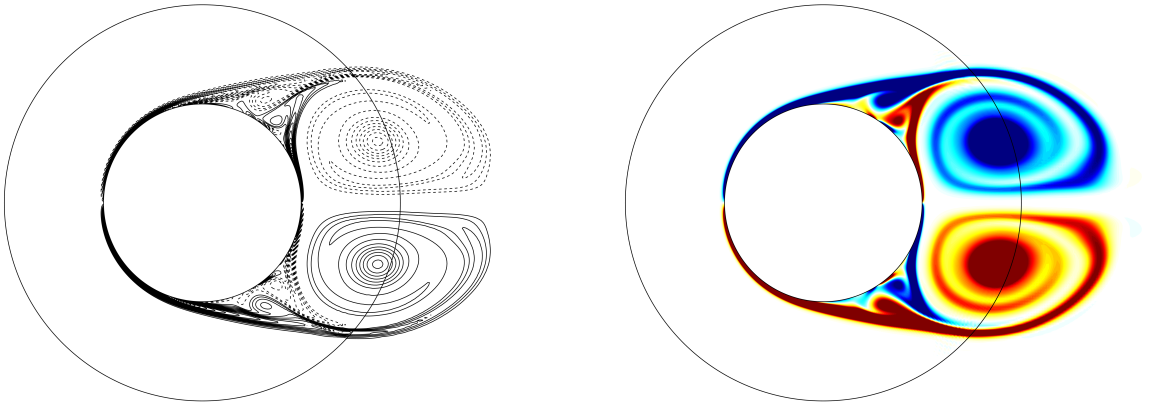


Fig. 15: Impulsively-started cylinder at $Re = 3000$: contours of dimensionless vorticity at $t^* \simeq 4$ in the NW and VPM solvers. Contours levels are by steps of 3. The color plot is saturated for $|\omega^*| > 10$. The limit $\partial\Omega^{\text{outer}}_{\text{NW}}$ between the NW and VPM results is represented by a thin black line.

$Re = 9500$

The flow around the cylinder at $Re = 9500$ is presented in Fig. 18. Figure 19 shows the drag coefficient; the higher Reynolds number leads to a comparison with the more recent contributions with penalization and IIM techniques, the works of Rossinelli et al. [5] and Gillis et al. [14], respectively. Our result agrees with those two works, especially at early times. The penalization technique [5] exhibits the first deviation, between $t^* = 1$ and 2 with respect to the other two results. This is consistent with the lower-order treatment inherent to the penalization which, in spite of the multi-resolution adaptive grid (MRAG) used in that work, leads to a different prediction of the first separation and shedding; this evidently affects the subsequent dynamics. The IIM [14] and the present coupled approach exhibit an excellent agreement up to a time $t^* \simeq 2.2$. These two references use very refined grids: the penalization-MRAG technique and the IIM have effective resolutions 22.4 and 5.6 times finer in the wake, respectively. At the wall though, the $h^{n,\text{wall}}_{\text{NW}}$ of the present approach is 1.6 times coarser than the penalization-MRAG technique and 2.4 times finer than the IIM. The wall vorticity, shown in Fig. 20, confirms that the present work captures the physics in a fashion similar to that of Gillis et al. [14] albeit with peaks slightly less pronounced. The results of Koumoutsakos and Leonard [32] do not quite capture those, as they are at a lower resolution (Rossinelli et al. [5] do not provide wall vorticity as it is less readily available in their penalization approach).

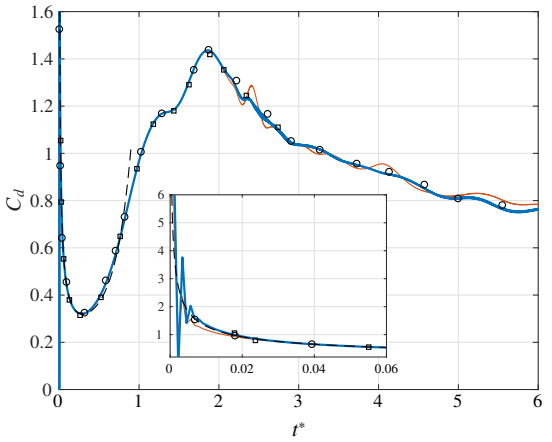


Fig. 16: Impulsively-started cylinder at $Re = 3000$: Drag coefficient. Present coupling: evaluation by the FD solver (—) and by Noca formula on a control surface situated at 1 D from the center of the cylinder (—). Gillis et al. [14] (○). Koumoutsakos and Leonard [32] (□). Theoretical curve [33] (– –).

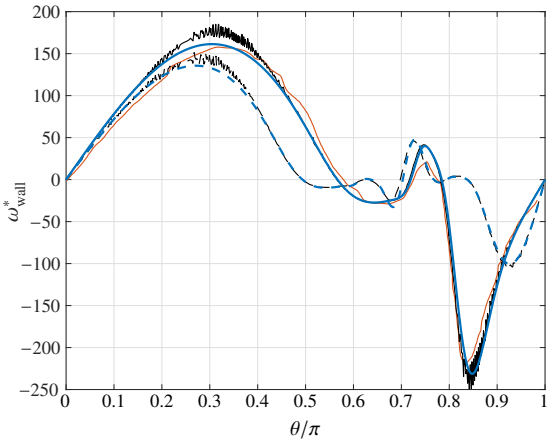
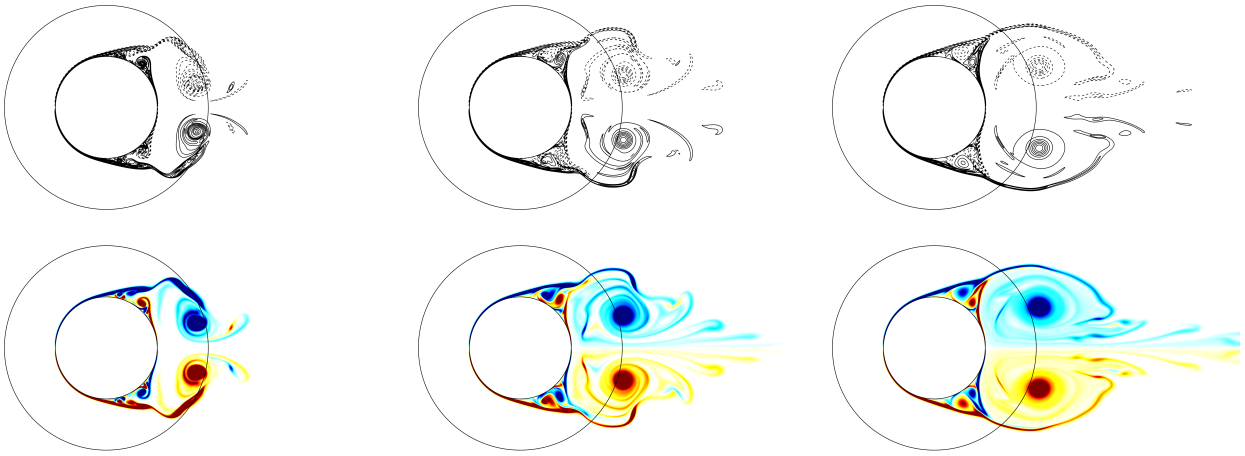


Fig. 17: Impulsively-started cylinder at $Re = 3000$: wall vorticity ω^*_{wall} vs the azimuthal position θ ($\theta = 0$ at the stagnation point). Present coupling ($t^* = 1$: —, $t^* = 3$: – –), Gillis et al. [14] ($t^* = 1$: —, $t^* = 3$: – –) and Koumoutsakos and Leonard [32] ($t^* = 1$: —).



(a) $t^* \simeq 3$ (b) $t^* \simeq 5$ (c) $t^* \simeq 7$

Fig. 18: Impulsively-started cylinder at $Re = 9500$: contours of dimensionless vorticity at $t^* \simeq 3$, 5, and 7 in the NW and VPM solvers. Contours levels are by steps of 6. The color plot is saturated for $|\omega^*| > 20$. The limit $\partial\Omega^{\text{outer}}_{\text{NW}}$ between the NW and VPM results is represented by a thin black line.

6.2. *Shedding regime*

We now consider the established periodic shedding regime at $Re = 200$ and 550. The NW mesh is again polar but differs from the impulsive start cases by its extent, 1 D from the wall. This longer distance allows the structures to diffuse more before reaching $\partial\Omega^{\text{outer}}_{\text{NW}}$ and thence for a coarser resolution of the VPM mesh, which extends up to 37D downstream of the cylinder.

Table 2 gathers the mesh parameters for the cases and the time resolution ratio between both solvers. Two resolutions are run for $Re = 200$ in order to assess resolution effects. We do not require the wall-normal mesh resolution $h^{n,\text{wall}}_{\text{NW}}$ to resolve the very thin boundary layers due to the impulsive start anymore; the constraint $h^+ < 1$ is thus only satisfied for the shedding regime. Most other parameters are set similarly to the impulsive start study. There

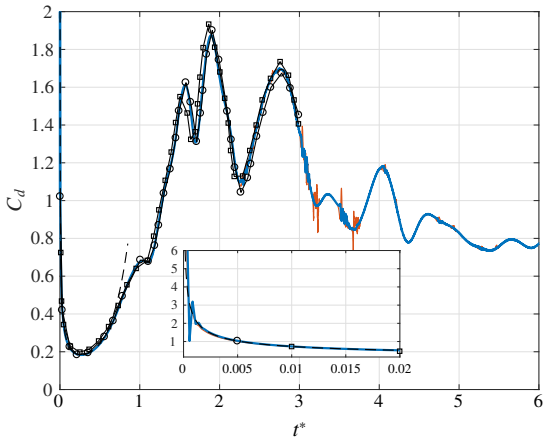


Fig. 19: Impulsively-started cylinder at $Re = 9500$: Drag coefficient. Present coupling: evaluation by the FD solver (—) and by Noca formula on a control surface situated at 1 D from the center of the cylinder (—). Gillis et al. [14] ( ). Rossinelli et al. [5] ( ). Theoretical curve [33] (- -).

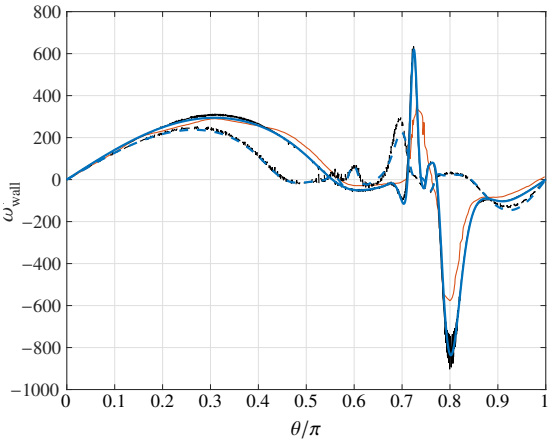


Fig. 20: Impulsively-started cylinder at $Re = 9500$: wall vorticity ω^*_{wall} vs the azimuthal position θ ($\theta = 0$ at the stagnation point). Present coupling ($t^* = 1$: —, $t^* = 3$: - -), Gillis et al. [14] ($t^* = 1$: —, $t^* = 3$: - -) and Koumoutsakos and Leonard [32] ($t^* = 1$: —).

are a few differences though: a small vertical freestream perturbation is added starting from $t^* = 0$ till $t^* = 1/\text{St}^2$, $U^y_\infty/U_\infty = 1/2 \sin(2\pi\ \text{St}\ t^*)$, to trigger shedding earlier and an outflow condition, $\partial\omega/\partial n = 0$, $\partial u_n/\partial n = 0$ and $u_s = 0$, is applied on the right boundary of the VPM Biot-Savart solver.

Table 2: Mesh parameters and ratio of temporal resolution between both solvers for the shedding cases.

Re	w/R	R/h_{VPM}	$R/h^{n,\text{wall}}_{\text{NW}}$	$h_{\text{VPM}}/h^{n,\text{wall}}_{\text{NW}}$	$h^{\theta,\text{wall}}_{\text{NW}}/h^{n,\text{wall}}_{\text{NW}}$	$\Delta t_{\text{VPM}}/\Delta t_{\text{NW}}$ (min..**avg**..max)
200_{coarse}	2	6.4	50	7.8	2.6	2..**2**..2
200_{fine}	2	12.8	100	7.8	2.6	2..**3**..3
550	2	12.8	100	7.8	2.6	2..**2**..2

$Re = 200$

From Fig. 21, we first observe the very good consistency of the vorticity field across the boundary $\partial\Omega^{\text{outer}}_{\text{NW}}$ in spite of the coarse resolution for the VPM solver. The effects of the mesh resolution and of the extent of the control surface $\partial\Omega_c$ on the force evaluations are highlighted in Fig. 22. The coarse resolution $R/h_{\text{VPM}} = 6.4$ exhibits marked oscillations in the VPM-based force measurements. The oscillations actually have a pattern following the redistribution frequency $N_r = 5$ of the second particle subset; this leads us to the assumption that their amplitude is also affected by the local flow distortion. The noise is markedly reduced for the 2 D control surface compared to larger surfaces; this is consistent with its computation being more governed by the subset-1 region and thus showing less the influence of the $N_r = 5$ numerical noise. Nevertheless, even at 2 D, the VPM-based predictions always present an offset with respect to the NW estimation. The fine resolution exhibits smaller oscillations and smaller offset than the coarse one thanks to the decreased distortion; from the coarse to the fine resolution, the time step was indeed decreased by a factor two while keeping the remeshing frequency constant.

Table 3 compares the lift coefficient C_l, drag coefficient C_d and Strouhal number St computed from wall quantities in the NW solver with those obtained when performing the same simulation with the NW solver alone (on a very finely resolved and wide domain, see Appendix C for the computational parameters), and with the literature. The results obtained with the coarse mesh are quite close to those produced by the fine mesh, indicating that they might

[2] St is the Strouhal number that can be found in well-known experimental curves [34]

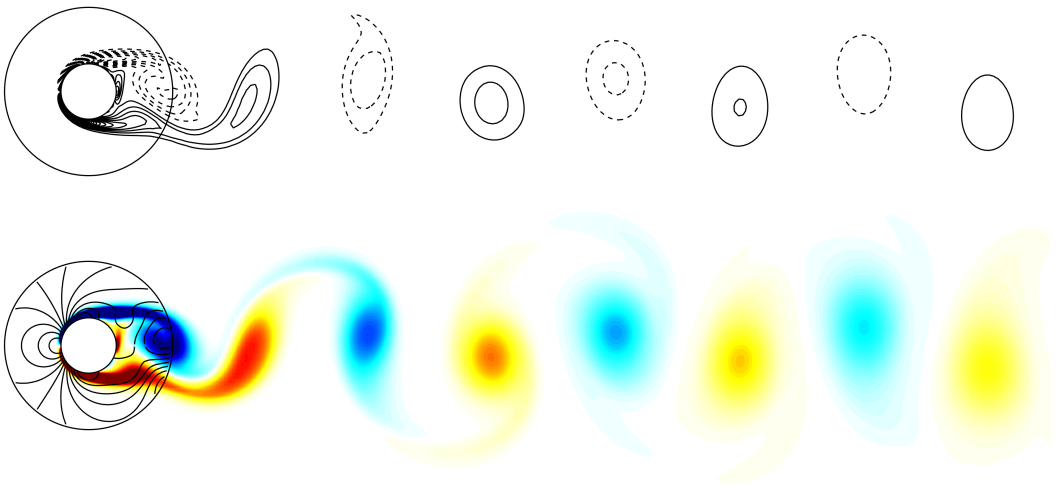


Fig. 21: Shedding past a cylinder at $Re = 200$ on the coarse resolution: contours of dimensionless vorticity and pressure (bottom) at $t^* \simeq 232$ in the NW and VPM solvers. Levels for ω^* are by steps of 1, while those for P^* are by steps of 0.2 and starts from P^*_{max}. The color plot is saturated for $|\omega^*| > 4$. The limit $\partial\Omega^{\text{outer}}_{\text{NW}}$ between the NW and VPM results is represented by a thin black line.

be already quite converged. The agreement with the uncoupled NW solver is very good, and so is it with the literature references. Moreover, the convergence studies performed in Section 5 indicate that the present fine results are clearly better converged than the coarse ones. The first two references [35, 36] use a Finite Volume method and their outer boundary are located at $30D$ and $50D$, respectively, from the center of the cylinder. Their mesh resolutions are quite coarse; 200×120 quadrilaterals are used to discretize the entire computational domain in [35], while only 81 points are used radially in [36]. The normal stretching for the latter is such that the normal resolution h_i^n/R increases from $\simeq 1/35$ at the wall to $\simeq 4$ at the outer boundary. The third reference [37] uses Finite Difference coupled with an IIM method to handle the body. The size of the computation domain, $80D \times 80D$, is discretized using 321×321 cells. An uniform 81×81 square mesh ($h_i^n/R \simeq 1/40$) is used in the $D \times D$ volume surrounding the cylinder. This mesh is next stretched to the inflow, outflow and far-field boundaries.

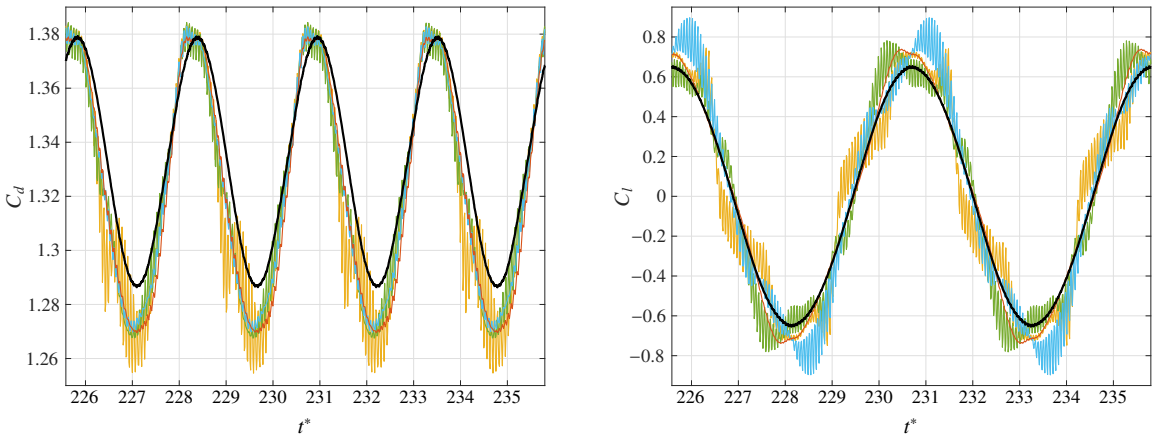
Table 3: Shedding past a cylinder at $Re = 200$: force coefficients and Strouhal number computed at the wall by the NW solver

	C_d	C_l	St
Present coupling (coarse)	1.333 ± 0.046	± 0.649	0.1957
Present coupling (fine)	1.328 ± 0.046	± 0.655	0.1952
NW solver alone	1.327 ± 0.0455	± 0.675	0.195
Wright and Smith [35] (Finite Volume)	1.33 ± 0.04	± 0.68	0.196
Rosenfeld et al. [36] (Finite Volume)	1.31 ± 0.04	± 0.65	0.20
Choi et al. [37] (Finite Difference + IIM)	1.36 ± 0.048	± 0.64	0.191

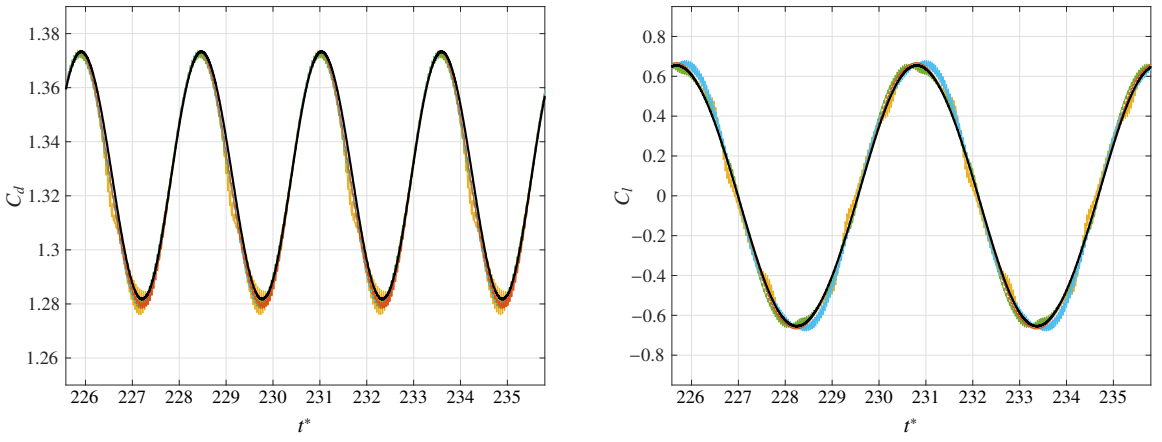
$Re = 550$

The results for the dynamics of the shedding regime at $Re = 550$ are scarce in the literature. Rather than for verification purposes, we here document this case for the sake of completeness. We ran this case up to $t^* = 400$, which corresponds to about 91 shedding periods. The vorticity contours, shown in Fig. 23, again indicate the good continuity of vorticity between the solvers, even though VPM is working at the same resolution as for the $Re = 200$ fine case.

The force coefficients shown in Fig. 25 show a good agreement between the NW and VPM-based estimations, in spite of the relatively low VPM resolution. The numerical noise for the larger control surfaces is also quite contained. Caution has to be used in the discussion of the force diagnostics and Strouhal number, though. The von Karman vortex street at this Reynolds number is indeed more unstable and the VPM domain is long enough to capture the



(a) Low resolution: $R/h_{\text{VPM}} = 6.4$ and $h_{\text{VPM}}/h_{\text{NW}}^{n,\text{wall}} = 7.8$



(b) High resolution: $R/h_{\text{VPM}} = 12.8$ and $h_{\text{VPM}}/h_{\text{NW}}^{n,\text{wall}} = 7.8$

Fig. 22: Shedding past a cylinder at $Re = 200$: evaluation of C_d and C_l by the NW solver (—) and by Noca formula on control surfaces situated at $2\,D$ (—), $5\,D$ (—), $10\,D$ (—) and $20\,D$ (—) from the center of the cylinder.

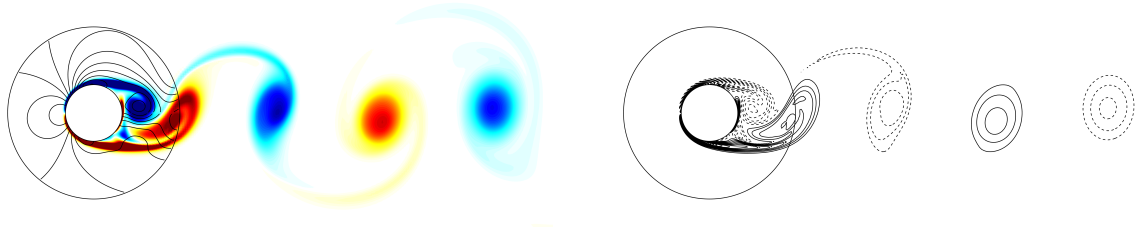


Fig. 23: Shedding past a cylinder at $Re = 550$ - zoom on $8D$ past the cylinder: contours of dimensionless vorticity and pressure (left) at $t^* \simeq 392$ in the NW and VPM solvers. Levels for ω^* are by steps of 1.5, while those for P^* are by steps of 0.3 and starts from P^*_{max}. The color plot is saturated for $|\omega^*| > 6$. The limit $\partial\Omega_{\text{NW}}^{\text{outer}}$ between the NW and VPM results is represented by a thin black line.

instability of this primary vortex street. It transitions to a secondary vortex street (see Fig. 24 a)) through vortex mergers. The breakdown of the primary Karman street is associated with the region of more intense dipole moment density that can be highlighted through the averaging over a sufficient number of shedding periods (here the last 65 periods of the simulation) of the vorticity and axial velocity fields, as shown in Fig. 24 b) and c). This dipole is located at a downstream distance of $24\,D$ approximately. This value is in agreement with the study of Dynnikova et al. [38]. The frequencies of the primary and secondary streets are measured using several probes positioned in the

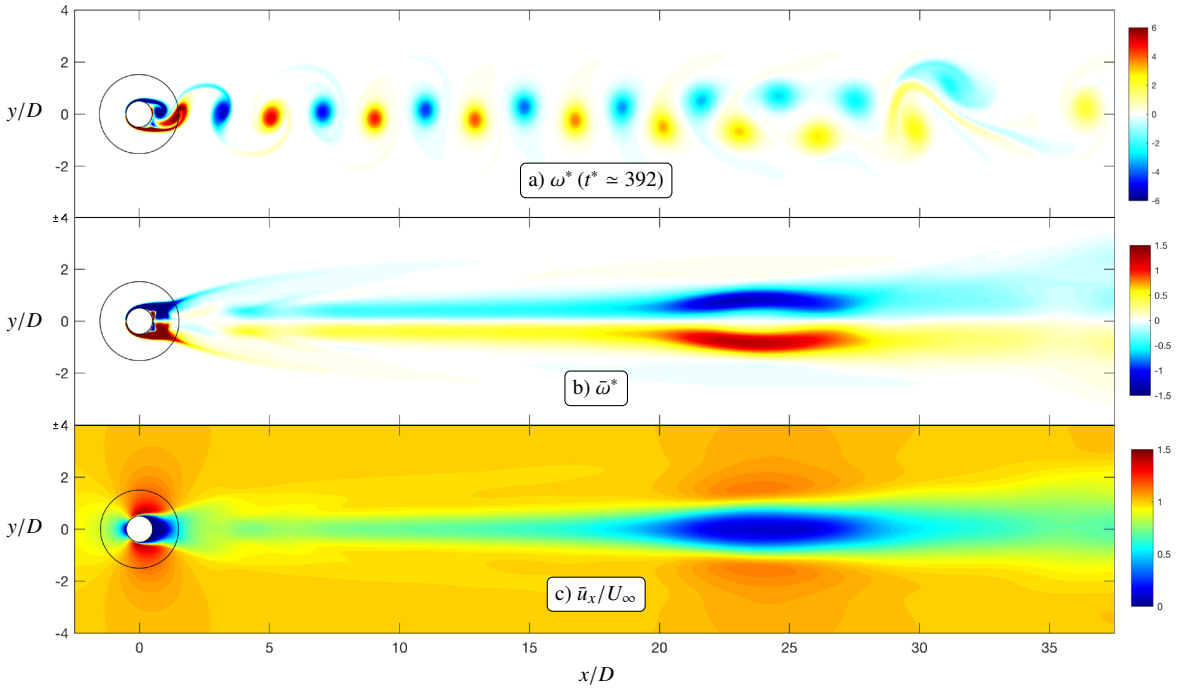


Fig. 24: Shedding past a cylinder at $Re = 550$: a) dimensionless vorticity at $t^* \simeq 392$. b) dimensionless vorticity averaged on the last 65 Strouhal periods. c) dimensionless axial velocity averaged on the last 65 Strouhal periods. The limit $\partial\Omega_{\mathrm{NW}}^{\mathrm{outer}}$ between the NW and VPM results is represented by a thin black line.

wake with a 1 D offset from the center line. From those, one can compute the Strouhal number of the primary street, $\mathrm{St}_1 = f_1 U_\infty / D \simeq 0.2272$, and the ratio between the primary and secondary frequencies: $\mathrm{St}_2/\mathrm{St}_1 = f_2/f_1 \simeq 0.3076$. The primary Strouhal number obtained matches quite well the common experimental data [34]. The frequency of the second street, while in agreement with Cimbala et al. [39], should be considered with caution given the proximity of the vortex street transition with the outflow boundary condition.

We have to point out that a very weak low-frequency oscillation, $f^* = f U_\infty / D \ll 1$, is also present in the time history of the force coefficients: $\Delta C_l = \Delta C_d \simeq 10^{-2}$. This oscillation, which can only be observed on a much larger period than Fig. 25, is likely due to the short extent available for the secondary vortex street to develop before encountering the outflow plane. For this reason, Table 4 reports mean lift and drag coefficients, as well as their respective minimal and maximal values, which have been averaged over the last 65 shedding periods.

Table 4: Shedding past a cylinder at $Re = 550$: force coefficients and Strouhal number computed at the wall by the NW solver.

$\bar{C}_d$	$\bar{C}_d^{min}$	$\bar{C}_d^{max}$	$\bar{C}_l$	$\bar{C}_l^{min/max}$	St_1
1.427	1.272	1.568	−0.004	± 1.177	0.2272

7. Application

The coupling methodology is applied to the flow past an impulsively-started regularized Joukowsky airfoil at an angle-of-attack (AoA) of 20° and at $Re \triangleq (U_\infty c)/\nu = 5000$, with c the airfoil chord. We note that this airfoil is regularized: its trailing edge has a non-zero thickness thanks to a modification of the conformal mapping from a cylinder. This regularization is such that the radius of curvature at the trailing edge is $r_t \simeq c/400$. This configuration clearly constitutes a forerunner of potential applications in wings, rotorcraft and biolocomotion studies.

The VPM domain extends up to 20 chords behind the airfoil and we run the simulation until $t^* \triangleq (t\, U_\infty)/c = 27$. The width of the NW domain varies between $0.4\,c$ and $0.65\,c$. Figure 26 provides a visual information about the

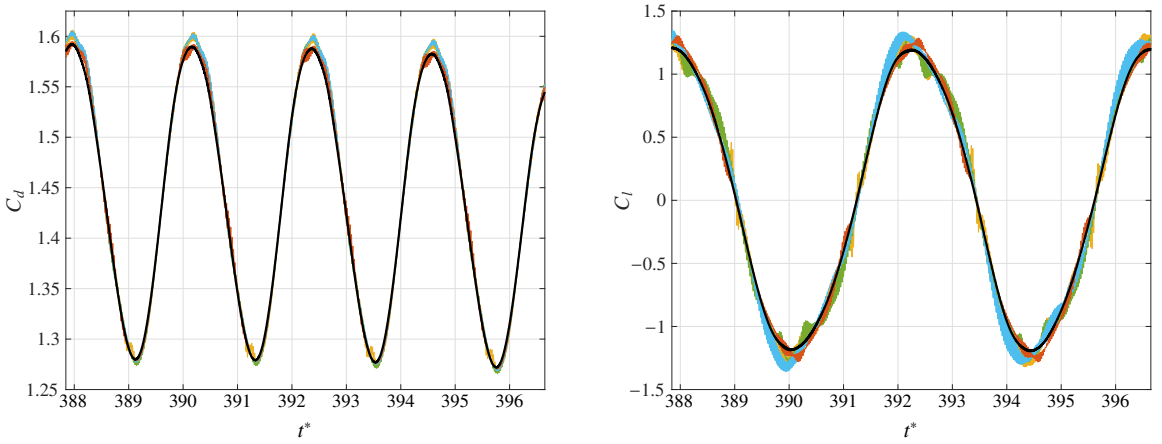


Fig. 25: Shedding past a cylinder at $Re = 550$: evaluation of C_d and C_l by the NW solver (—) and by Noca formula on control surfaces situated at $2\,D$ (—), $5\,D$ (—), $10\,D$ (—) and $20\,D$ (—) from the center of the cylinder.

mesh of the NW solver and its cell size with respect to the VPM mesh. We observe that the ratio between the NW mesh size at the wall and the VPM one, $h_{\text{VPM}}/h_{\text{NW}}^{\text{wall}}$, varies around the body: the resolution ratio is very large at the leading and trailing edges but less so on the suction and pressure sides. This varying resolution is required to capture the finest flow scales produced on the leading and trailing edges. More specifically, the presented NW wall cell sizes allow to maintain $h^+ < 2$ all along the simulation. The uniform VPM mesh size $h_{\text{VPM}} \simeq c/185$ is set up in such a way to capture the vortical structures leaving the overlapping NW domain. The NW mesh stretching is designed to approximately match the VPM resolution on $\partial\Omega_{\text{NW}}^{\text{outer}}$ as for the verification cases. The ratio between the time steps of the two solvers, $\Delta t_{\text{VPM}}/\Delta t_{\text{NW}}$, varies between 3 and 8. Had it not been for the implicit handling of the diffusive term in the NW solver, this ratio would have been 15 times larger. The VPM solver again uses an outflow condition as in Section 6.2.

Figure 27 provides some insights into the vortex dynamics at play in the early times of this flow. One can clearly see the startup vortex emerging from the trailing edge at $t^* = 1$; it is followed by a thin wake composed of the vorticity generated in the pressure and suction sides ($t^* = 2$). As the flow goes through complex separations on the suction side, the conservation of circulation imposes a net non-zero vorticity flux across the two lobes of this thin wake. This gives rise to Kelvin-Helmholtz-like instabilities ($t^* = 2$ to 4) and the shedding of distinct vortices with positive circulation. Meanwhile, on the suction side, the separated boundary layers have coalesced into a large vortex that gets shed around $t^* \simeq 4.5$. This negative vortex greatly affects the flow in the vicinity of the trailing edge. The flow separates at a sharp angle with respect to the trailing edge and the pressure side boundary layer thus rolls up into a positive vortex above the airfoil; this vortex will be shed around $t^* \simeq 5.5$.

Such shedding events are clearly indicative of large force variations, as it will be confirmed further below, and actually, are going to repeat during the regime phase, shown in Fig. 28. The subsequent wake, which consists of these unevenly shed vortices, gives rise to pairing events and the ejection of several counter-rotating pairs away from the main axis of the wake and at random angles. Additionally, the curved trajectories and the rotation of these pairs reveals that their vortices do not have perfectly opposite strengths. The random or chaotic character of these pairing and ejection events clearly begs for a deeper analysis, which we leave as a subject of future work.

With the exception of a few small oscillations, the forces, shown in Fig. 29, again exhibit a very good agreement between the NW and VPM components, for any control surface. This confirms, on a quite complex case, that the coupling algorithm can accommodate non-trivial overlapping configurations between the NW and VPM meshes.

8. Conclusions and perspectives

We have introduced a novel coupling methodology to combine a vortex particle-mesh method with a near-wall body-fitted velocity-pressure solver toward the efficient simulation of two-dimensional aerodynamics problems and of their wakes. The proposed coupling relies on accurate and robust two-way exchanges of information between the

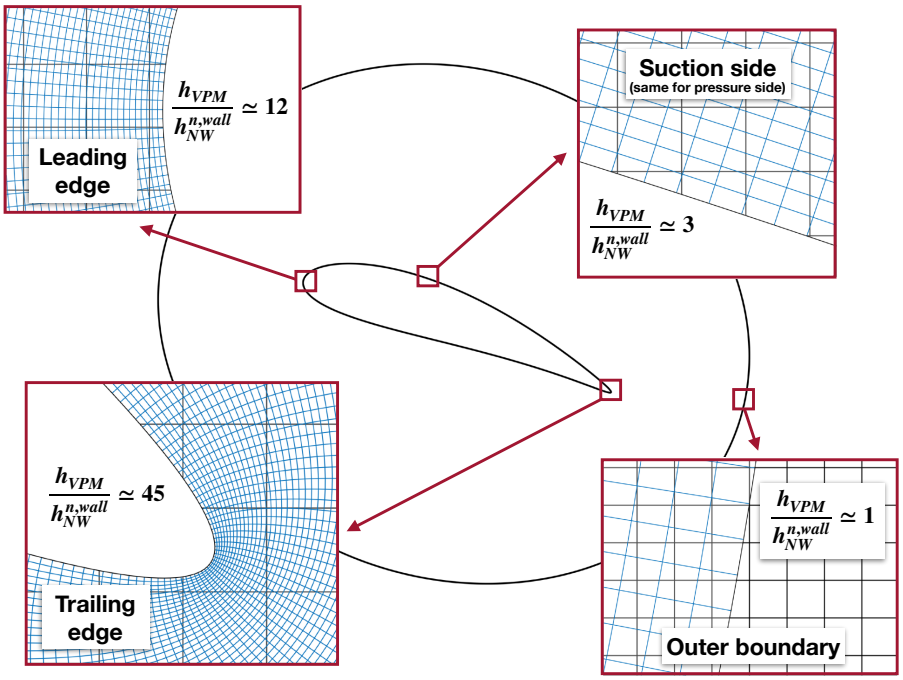


Fig. 26: Mesh for the airfoil case.

solvers. From the NW solver to VPM solver, the method interpolates the NW velocity field to compute a vorticity correction inside VPM. As this correction consists in the FD curl of a velocity, it conserves the circulation around the object up to an interpolation error. The transfer of information from VPM solver to the NW solver is performed through mixed boundary conditions that preserve the vorticity flux for the NW solver. These exchanges are therefore non-intrusive for the component solvers and do not involve computationally-intensive Schwartz iterations. Additionally, the method does not require the enforcement of a wall boundary condition within VPM time stepping, nor any circulation accounting.

Our results indicate that the coupling of the two second-order component solvers, the FD and VPM solvers, achieves itself a global, i.e. at constant CFL, second-order convergence. The test cases of the flow past a cylinder and airfoil have demonstrated the synergetic performance of the method, with the NW solver capturing boundary layers, from their inception to their separation and the VPM solver in charge of accurately advecting vortical structures far into the wake. The results show a very good agreement with the literature and confirm the numerical accuracy and robustness of the coupling.

In terms of perspectives, the method could benefit from filtering the NW solver velocity field prior to its interpolation on the staggered VPM interpolation grid (step 1 of the correction process). Indeed, sampling errors can appear through the interpolation and those are all the more important as the local mesh size of the NW mesh is small compared to the VPM mesh. Filtering could then help to recover a more meaningful (i.e. with less aliasing noise) corrected vorticity fields for the VPM solver in the near-wall region. Filtering had been found unnecessary for the present cases, still at moderate Reynolds numbers, but it could surely prove useful at very high Reynolds numbers.

The methodology does not exploit any property or hypothesis of two-dimensional flow. Hence, we do not foresee any fundamental hurdle in extending it to three dimensions. This discussion logically segues to the handling of higher Reynolds numbers and the addition of a sub-grid scale (SGS) model and the transition to a Large Eddy Simulation. Again, the present DNS results exhibit a good robustness to the discontinuity in resolution and formulation; this should most likely translate to the discontinuity in the SGS models active within the NW and VPM solvers. Such developments would also benefit from an adaptive mesh or multi-resolution [5, 40] for the VPM method: it would further increase the computational efficiency and automatize the flexible transition with the mesh resolution of the

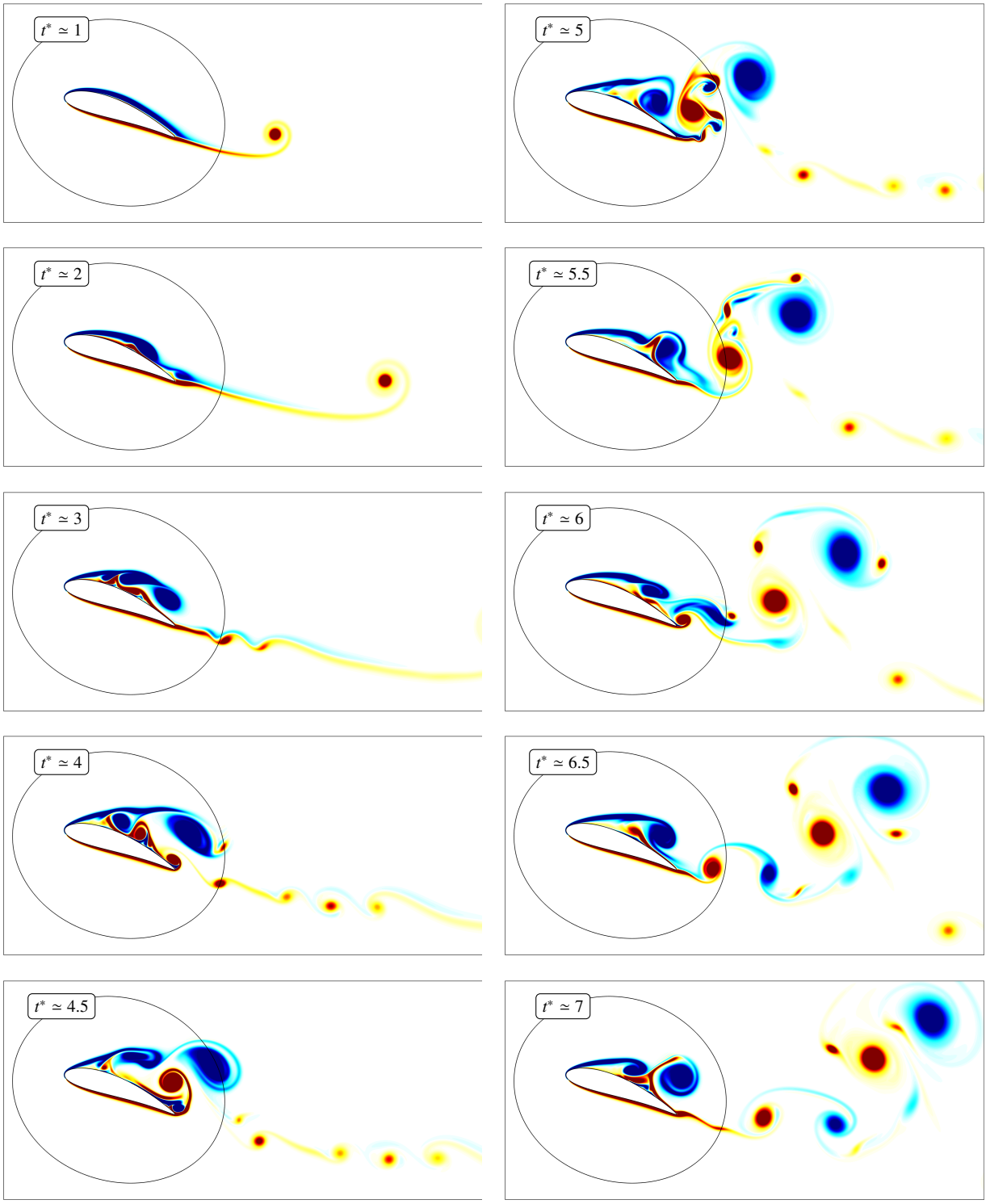


Fig. 27: Flow past the airfoil: dimensionless vorticity field $\omega^* \triangleq (\omega\, c)\,/U_\infty$ at several times. The plots are saturated for $\omega^* > 20$.

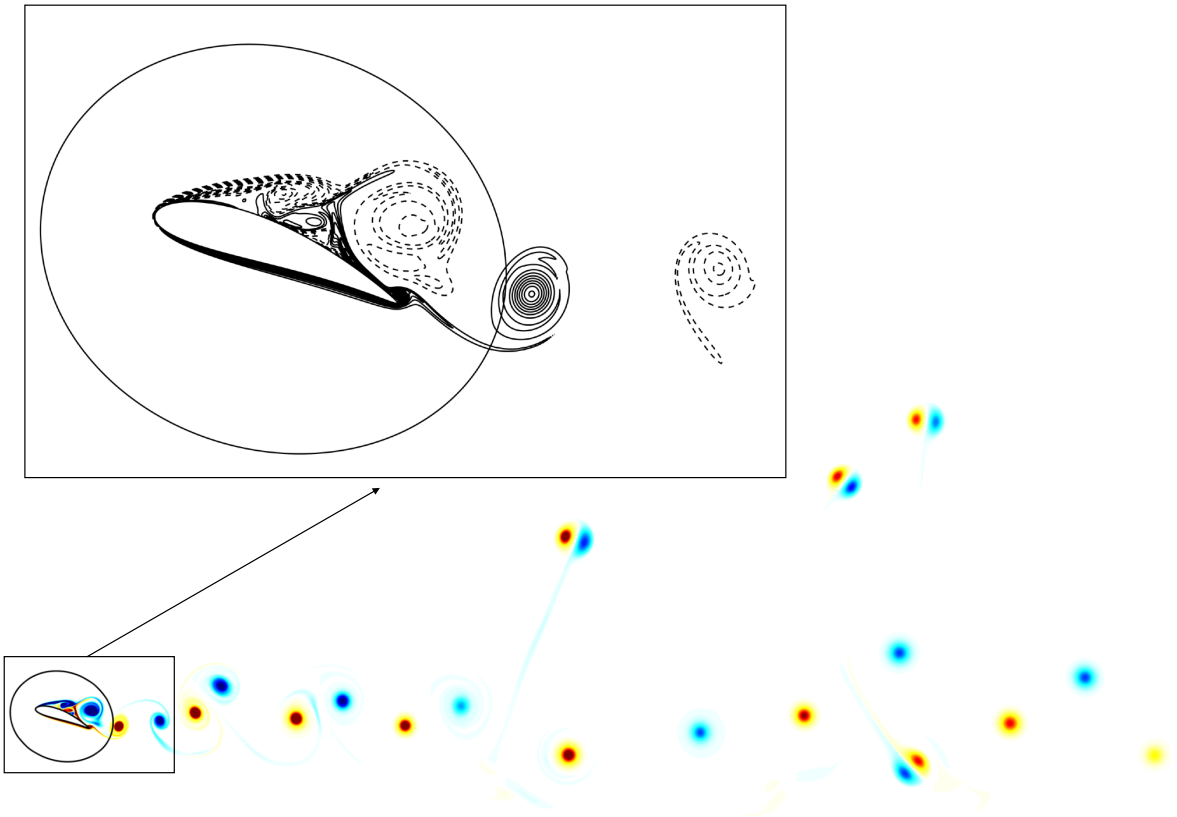


Fig. 28: Flow past the airfoil: dimensionless vorticity field $\omega^* \triangleq (\omega\, c)\,/U_\infty$ at $t^* \simeq 27$. The color plots are saturated for $\omega^* > 20$. Contours levels for the top-left image are by steps of 6.

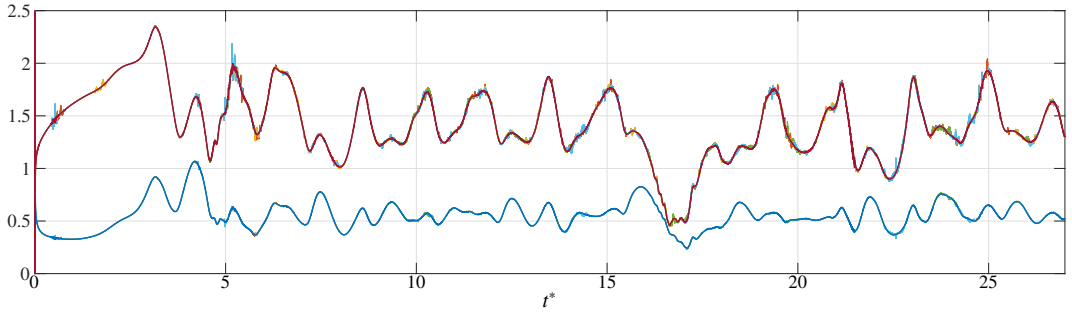


Fig. 29: Flow past the airfoil: evaluation of forces by the NW solver at the wall (C_d: —, C_l: —) and by Noca formula on control surfaces situated at 1 c (—), 2 c (—), 5 c (—) and 10 c (—) from the center of the airfoil.

NW solver.

The handling of moving and deforming boundaries mostly involves computational developments on the side of the NW solver, e.g. an Arbitrary Lagrangian-Eulerian (ALE) mesh, a time-varying overlap with the VPM mesh, etc. For the VPM solver, it will require small additions that can be seen as natural extensions of the present work. Indeed, let us recall that, in the general case, the VPM solver relies on a Helmholtz decomposition of the velocity field $\boldsymbol{u} = \boldsymbol{U}_\infty + \boldsymbol{u}_\omega + \boldsymbol{u}_\sigma$, where the non-solenoidal component is given by $\boldsymbol{u}_\sigma = \nabla\phi$ with $\nabla^2\phi = \sigma \triangleq \nabla\cdot\boldsymbol{u}$. For a generic deforming body, the deformation velocity field is not necessarily divergence-free inside the body, $\nabla\cdot\mathbf{u}_{\mathrm{VPM,corr}} \neq 0$ and the non-solenoidal component of the Helmholtz decomposition is thus non-zero also outside the body. As a result, one also has to compute the divergence of the correction velocity and solve the Poisson equation for the scalar potential ϕ, see, e.g., a similar treatment in [11].

To conclude then, the present coupling clearly sets the stage for the high fidelity and efficient simulation of flows with wake-device interactions in domains going from aircraft and rotorcraft aerodynamics, wind turbines, and bio-locomotion.

9. Acknowledgments

Computational resources have been provided by the Consortium des Équipements de Calcul Intensif (CÉCI), funded by the Fonds de la Recherche Scientifique de Belgique (F.R.S.-FNRS) under Grant n° 2.5020.11 and by the Walloon Region. The present research also benefited from computational resources made available on the Tier-1 supercomputer of the Federation Wallonie-Bruxelles, infrastructure funded by the Walloon Region under the grant agreement n° 1117545.

Appendix A. Specificities about the Finite Difference NW solver

The Finite Difference NW solver used in this coupling approach is only able to handle orthogonal meshes. Those are obtained by performing a conformal mapping starting from an uniform rectangular grid (see Fig. A.30). This uniform grid is what we call the *computational domain*, while the target orthogonal grid is called the *physical domain*. Let us denote (n, s) the coordinates of a specific node in the computational domain and (x, y) the node in the physical domain. The position in the physical domain of a specific node in the computational domain is obtained by applying the conformal mapping describing the mesh : $(x, y) = f(n, s)$. And, conversely, the position in the computational domain of a specific node in the physical domain is obtained by applying the inverse transformation : $(n, s) = f^{-1}(x, y)$. The left edge of the computational domain corresponds to the wall, and the no-slip and no-through flow boundary conditions are enforced on it. Periodic boundary conditions are enforced on the upper and lower edges. The right edge corresponds to $\partial\Omega^{\mathrm{outer}}_{\mathrm{NW}}$ and the mixed Dirichlet and Neumann-type conditions (see Section 3.1) are enforced there.

The spatial operators are written in the local orthogonal frame of each cell, and based on the (n, s) orthogonal coordinates system from the computational domain. This leads to a velocity, pressure and vorticity fields expressed in (1) (n, s) orthogonal coordinates and (2) local orthogonal components for the velocity field (tangential u_s and normal u_n components). The Navier-Stokes equations strictly speaking are therefore not discretized in the physical domain but in the computational domain. The expressions of those operators are based on classical definitions of metrics $h_n = \|\partial\boldsymbol{x}/\partial n\|$ and $h_s = \|\partial\boldsymbol{x}/\partial s\|$, and of the unit vectors $\hat{\boldsymbol{e}}_n = h_n^{-1}\partial\boldsymbol{x}/\partial n$ and $\hat{\boldsymbol{e}}_s = h_s^{-1}\partial\boldsymbol{x}/\partial s$. The expressions of those operators can be easily derived [41, 42]. For the sake of clarity, we provide hereunder the operators discretized in the NW solver; i.e., the expressions for the convective term, $\boldsymbol{H} \triangleq (\boldsymbol{u}\cdot\nabla\boldsymbol{u})$, the gradient of a scalar ϕ, $\nabla\phi$, the rotational of the velocity field, $\omega \triangleq \nabla\times\boldsymbol{u}$, the Laplacian of the velocity field, $\nabla^2\boldsymbol{u}$, the divergence of the predictor velocity field $\boldsymbol{u}^*$, $\nabla\cdot\boldsymbol{u}^*$, and the Laplacian of a scalar g, $\nabla^2 g$:

$$\boldsymbol{H} = \left\{\frac{u_n}{h_n}\frac{\partial u_n}{\partial n} + \frac{u_s}{h_s}\frac{\partial u_n}{\partial s} + \frac{u_s}{(h_n h_s)}\left(u_n\frac{\partial h_n}{\partial s} - u_s\frac{\partial h_s}{\partial n}\right)\right\}\hat{\boldsymbol{e}}_n + \left\{\frac{u_n}{h_n}\frac{\partial u_s}{\partial n} + \frac{u_s}{h_s}\frac{\partial u_s}{\partial s} + \frac{u_n}{(h_n h_s)}\left(u_s\frac{\partial h_s}{\partial n} - u_n\frac{\partial h_n}{\partial s}\right)\right\}\hat{\boldsymbol{e}}_s \quad \text{(A.1)}$$

$$\nabla\phi = \left\{\frac{1}{h_n}\frac{\partial\phi}{\partial n}\right\}\hat{\boldsymbol{e}}_n + \left\{\frac{1}{h_s}\frac{\partial\phi}{\partial s}\right\}\hat{\boldsymbol{e}}_s \quad \text{(A.2)}$$

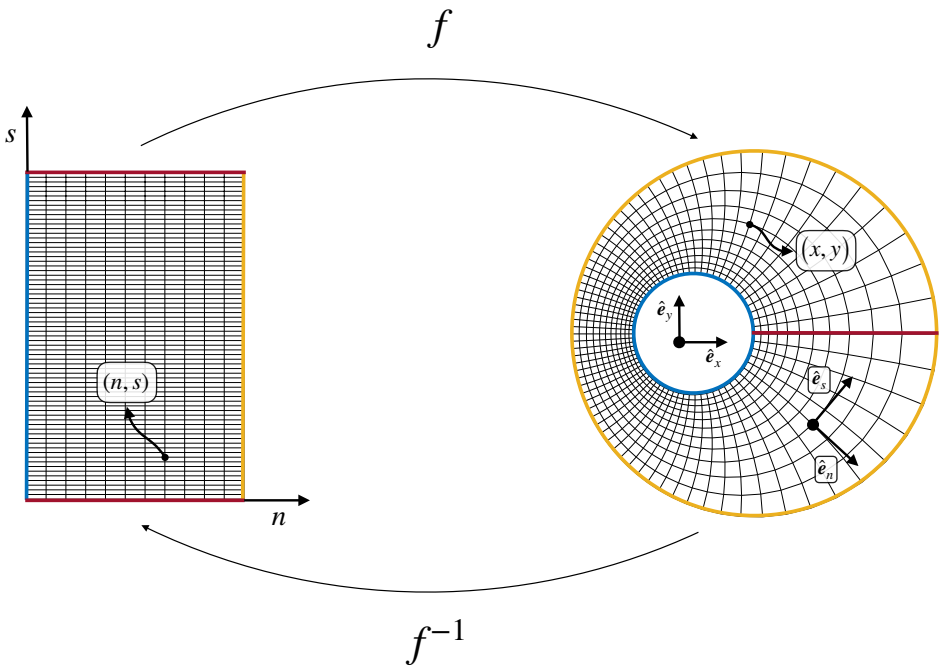


Fig. A.30: Direct and inverse mapping between the computational (left) and the physical (right) domains. Boundary conditions: wall (—), mixed Dirichlet and Neumann-type condition (—) on $\partial\Omega_{\mathrm{NW}}^{\mathrm{outer}}$, and periodic condition (—).

$$\omega = \frac{1}{(h_n\, h_s)}\left\{\frac{\partial}{\partial n}\left(h_s\, u_s\right) - \frac{\partial}{\partial s}\left(h_n\, u_n\right)\right\} \tag{A.3}$$

$$\nabla^2 \boldsymbol{u} = \nabla \underbrace{(\nabla \cdot \boldsymbol{u})}_{0} - \nabla \times \omega = -\frac{1}{h_s}\left\{\frac{\partial \omega}{\partial s}\right\} \hat{\boldsymbol{e}}_n + \frac{1}{h_n}\left\{\frac{\partial \omega}{\partial n}\right\} \hat{\boldsymbol{e}}_s \tag{A.4}$$

$$\nabla \cdot \boldsymbol{u}^* = \frac{1}{(h_n\, h_s)}\left\{\frac{\partial}{\partial n}\left(h_s\, u_n^*\right) + \frac{\partial}{\partial s}\left(h_n\, u_s^*\right)\right\} \tag{A.5}$$

$$\nabla^2 g = \frac{1}{(h_s\, h_s)}\left\{\frac{\partial}{\partial n}\left(\frac{h_s}{h_n}\frac{\partial g}{\partial n}\right) + \frac{\partial}{\partial s}\left(\frac{h_n}{h_s}\frac{\partial g}{\partial s}\right)\right\} \tag{A.6}$$

Appendix A.1. Lagrange interpolation

A Lagrange interpolation from the NW mesh onto a staggered version of the VPM grid is carried out in Step 1 of the correction process (Section 3.3). This interpolation is performed on the computational domain and not on the physical domain. More precisely, from a specific position (x, y) in the physical domain, we first retrieve the corresponding coordinates in the computational domain via the inverse transformation : $(n, s) = f^{-1}(x, y)$. Secondly, we interpolate the field from the uniform rectilinear computational grid onto the specific point (n, s) using third order Lagrange polynomials based on the nearest grid points. This interpolation is always centered in the $\hat{\boldsymbol{e}}_s$ direction (thanks to the periodicity in this direction). In the $\hat{\boldsymbol{e}}_n$ direction, the interpolation is centered when geometrically possible only; a partial decentering will arise for points located within cells adjacent to the wall or $\partial\Omega_{\mathrm{NW}}^{\mathrm{outer}}$.

Appendix B. Convergences studies: mesh parameters for the NW solver and error data

Appendix B.1. NW mesh

The orthogonal eccentric NW mesh used for the convergence studies (see Fig. 8) is obtained through the following conformal transformation of a polar mesh:

$$z = R\left(\frac{\frac{Z}{R} + \lambda}{1 + \lambda\,\frac{Z}{R}}\right) \tag{B.1}$$

where Z and z are the complex positions in the initial polar mesh and the eccentric mesh after the transformation, respectively. We aim to map the annular polar mesh defined from $r = R$ to $r = r_{out}$ into a mesh for which the inner circle $r = R$ remains the same but the eccentricity defined by $e \triangleq |\boldsymbol{x}_c^o - \boldsymbol{x}_c^i|/D$ is equal to 0.5 and the outer diameter is three times larger than the inner one, $D_o/D_i = 3$. The mapping parameters that achieve these geometrical constraints, λ and the radial extension r_{out} of the initial polar mesh, can be expressed in terms of the eccentricity and the diameters ratio D_o/D_i as

$$\lambda = \frac{1}{4e}\left[\sqrt{\left(\left[\frac{D_o}{D_i}\right]^2 - [2e-1]^2\right)\left(\left[\frac{D_o}{D_i}\right]^2 - [2e+1]^2\right)} - \left(\frac{D_o}{D_i}\right)^2 + 4e^2 + 1\right] \simeq -0.146 \tag{B.2}$$

$$\frac{r_{out}}{R} = \frac{1}{2\frac{D_o}{D_i}}\left[\sqrt{\left(\left[\frac{D_o}{D_i}\right]^2 - [2e-1]^2\right)\left(\left[\frac{D_o}{D_i}\right]^2 - [2e+1]^2\right)} + \left(\frac{D_o}{D_i}\right)^2 - 4e^2 + 1\right] \simeq 2.62 \tag{B.3}$$

Table B.5 presents the key mesh parameters for the NW meshes used in the convergence study; we provide the mesh discretization along the normal and tangential directions ($N_n \times N_\theta$), the first cell size at the wall $h^n_{wall} = h^n_0$ and the stretching in the normal direction h^n_{i+1}/h^n_i for the initial polar mesh. For each resolution, the stretching factor is computed in such a way the outer edge of the last cell ends exactly at r_{out}; i.e., by solving the following equation:

$$r_{out} - R = h^n_{wall}\sum_{i=0}^{N_n-1}\left(\frac{h^n_{i+1}}{h^n_i}\right)^i \tag{B.4}$$

The stretching is thus essentially performed on the polar mesh, then only the conformal mapping is applied. The expression of the complex position in the initial polar mesh based on (n, s) coordinates from the computational domain is $Z = r(n)\,e^{i\,s}$ where the expression for the radius is :

$$r(n) = R + \frac{h^n_{wall}}{\left[\left(\frac{h^n_{i+1}}{h^n_i}\right) - 1\right]}\left[\left(\frac{h^n_{i+1}}{h^n_i}\right)^{\frac{n}{\Delta n}} - 1\right] \tag{B.5}$$

where Δn is the uniform resolution in the computational domain of the n coordinate.

$N_n \times N_\theta$	h^n_{wall}/R	h^n_{i+1}/h^n_i
22×140	4e-2	$\simeq 1.054$
$\times 2$	$\div 2$	$\simeq 1.0262$
$\times 4$	$\div 4$	$\simeq 1.0129$
$\times 8$	$\div 8$	$\simeq 1.00639$
$\times 16$	$\div 16$	$\simeq 1.00318$

Table B.5: Mesh parameters for the NW polar mesh before applying the conformal mapping.

[3] Note that the n upper-script in h^n_{i+1}/h^n_i and h^n_{wall} expressions do not correspond to the n coordinate from the computational domain but only highlights the normal direction of these cell sizes.

Appendix B.2. Error data

Tables B.6, B.7, B.8, and B.9 gather the values of the errors E_2 and E_∞ obtained for the different convergence studies, and also the local slopes r_2 and r_∞. The spatial resolution, temporal resolution, and the Fourier number (r) are also provided. For the latter, we either provide the maximal value attained on the non-uniform mesh of the NW solver (r_{max}), or the constant value in the case of the uniform mesh VPM solver (r). The temporal resolution is made dimensionless using the characteristic velocity $U \triangleq \frac{\Gamma}{2\pi R}$. For the VPM solver, we provide also the two common accuracy criteria: $|\boldsymbol{S}|_{max}\,\Delta t$ and $|\omega_{max}|\,\Delta t$.

$N_n \times N_\theta$	$(U\,\Delta t)\,/D$	r_{max}	$E_2^{\boldsymbol{u}}$	$r_2^{\boldsymbol{u}}$	$E_\infty^{\boldsymbol{u}}$	$r_\infty^{\boldsymbol{u}}$	E_2^{ω}	r_2^{ω}	E_∞^{ω}	r_∞^{ω}	E_2^{P}	r_2^{P}	E_∞^{P}	r_∞^{P}
22 × 140	2.55e-2	0.212	4.03e-5		2.33e-5		7.58e-5		1.68e-4		1.31e-6		4.39e-7	
×2	÷2	0.424	9.7e-6	2.06	5.75e-6	2.02	1.88e-5	2.01	4.19e-5	2.0	3.23e-7	2.02	1.08e-7	2.02
×4	÷4	0.848	2.38e-6	2.03	1.43e-6	2.01	4.67e-6	2.01	1.05e-5	2.0	8.0e-8	2.01	2.68e-8	2.01
×8	÷8	1.696	5.9e-7	2.01	3.55e-7	2.01	1.17e-6	2.0	2.62e-6	2.0	1.99e-8	2.01	6.68e-9	2.01
×16	÷16	3.391	1.47e-7	2.01	8.85e-8	2.0	2.91e-7	2.0	6.56e-7	2.0	4.96e-9	2.0	1.67e-9	2.0

Table B.6: Error data for the global convergence of the NW solver running alone.

$N_x \times N_y$	$(U\,\Delta t)\,/D$	r	$\lvert\boldsymbol{S}\rvert_{max}\Delta t$	$\lvert\boldsymbol{\omega}\rvert_{max}\Delta t$	$E_2^{\boldsymbol{u}}$	$r_2^{\boldsymbol{u}}$	$E_\infty^{\boldsymbol{u}}$	$r_\infty^{\boldsymbol{u}}$	E_2^{ω}	r_2^{ω}	E_∞^{ω}	r_∞^{ω}
256×256	2.55e-1	1.04e-2	1.34e-2	6.35e-2	1.74e-4		2.76e-5		8.03e-5		2.27e-5	
×2	÷2	2.09e-2	6.71e-3	3.18e-2	4.33e-5	2	6.84e-6	2.01	1.9e-5	2.08	5.2e-6	2.13
×4	÷4	4.17e-2	3.36e-3	1.59e-2	1.08e-5	2	1.71e-6	2	4.72e-6	2.01	1.36e-6	1.93
×8	÷8	8.34e-2	1.68e-3	7.96e-3	2.7e-6	2	4.27e-7	2	1.18e-6	2	3.6e-7	1.92
×16	÷16	0.17	8.4e-4	3.98e-3	6.75e-7	2	1.07e-7	2	2.94e-7	2	9.76e-8	1.88

Table B.7: Error data for the global convergence of the VPM solver running alone.

$N_n \times N_\theta$	$(U\,\Delta t)\,/D$	r_{max}	$E_2^{\boldsymbol{u}}$	$r_2^{\boldsymbol{u}}$	$E_\infty^{\boldsymbol{u}}$	$r_\infty^{\boldsymbol{u}}$	E_2^{ω}	r_2^{ω}	E_∞^{ω}	r_∞^{ω}	E_2^{P}	r_2^{P}	E_∞^{P}	r_∞^{P}
22 × 140	2.55e-2	0.212	4.11e-5		2.92e-5		4.96e-5		1.13e-4		7.82e-7		4.98e-7	
×2	÷2	0.424	9.88e-6	2.06	6.99e-6	2.06	1.23e-5	2.01	2.75e-5	2.04	2.14e-7	1.87	1.26e-7	1.98
×4	÷4	0.848	2.46e-6	2.0	1.76e-6	1.99	3.14e-6	1.97	6.95e-6	1.98	5.37e-8	2.0	3.16e-8	2.0
×8	÷8	1.696	6.32e-7	1.96	4.6e-7	1.94	8.24e-7	1.93	1.83e-6	1.92	1.3e-8	2.05	8.43e-9	1.91
×16	÷16	3.391	1.67e-7	1.91	1.22e-7	1.91	2.26e-7	1.87	5.2e-7	1.82	3.49e-9	1.9	2.28e-9	1.88

Table B.8: Error data for the global convergence of the coupling in the NW domain.

$N_x \times N_y$	$(U\,\Delta t)\,/D$	r	$\lvert\boldsymbol{S}\rvert_{max}\Delta t$	$\lvert\boldsymbol{\omega}\rvert_{max}\Delta t$	$E_2^{\boldsymbol{u}}$	$r_2^{\boldsymbol{u}}$	$E_\infty^{\boldsymbol{u}}$	$r_\infty^{\boldsymbol{u}}$	E_2^{ω}	r_2^{ω}	E_∞^{ω}	r_∞^{ω}
256×256	2.55e-1	1.04e-2	1.34e-2	6.34e-2	2.16e-4		3.47e-5		3.01e-5		1.5e-5	
×2	÷2	2.09e-2	6.71e-3	3.18e-2	5.5e-5	1.97	8.82e-6	1.98	1.31e-5	1.2	5.22e-6	1.53
×4	÷4	4.17e-2	3.36e-3	1.59e-2	1.39e-5	1.99	2.23e-6	1.99	3.94e-6	1.74	1.37e-6	1.93
×8	÷8	8.34e-2	1.68e-3	7.96e-3	3.48e-6	1.99	5.63e-7	1.98	1.05e-6	1.91	3.62e-7	1.92
×16	÷16	0.17	8.4e-4	3.98e-3	8.73e-7	2.0	1.43e-7	1.97	2.71e-7	1.95	9.8e-8	1.89

Table B.9: Error data for the global convergence of the coupling in the VPM-only domain.

Appendix C. Computational parameters for the NW solver alone for the shedding case at $Re = 200$

This simulation is performed on a wide and very finely resolved polar mesh (extending up to $40D$ behind the cylinder). On the outer boundary, the freestream velocity U_∞ and zero vorticity are enforced. Based on this boundary condition, we stop the simulation before any vortical structure reaches the outer boundary; i.e., at $t^* = 45$. The shedding is triggered using the same vertical freestream perturbation as for the coupling cases. At the end of the simulation, the shedding is converged up to $20 \sim 25D$ behind the cylinder, with the starting vortices located further downstream. This simulation is thus less accurate in terms of wake length with respect to the coupling cases but the resolution is better in the near-wall region (see table C.10 that gathers all the mesh parameters). The normal

resolution at the wall, $h_{\mathrm{NW}}^{n,\mathrm{wall}}$, is indeed 5 times finer than in the coarse coupling case (2.5 for the fine resolution). Regarding the tangential wall resolution, $h_{\mathrm{NW}}^{\theta,\mathrm{wall}}$, it is about 13.3 times finer than in the coarse coupling case (6.7 for the fine resolution). We note that this polar mesh and the stretching (h_{i+1}^n/h_i^n) are such that the resolutions in the normal and tangential directions remain finer than the coarse coupling case up to $19D$ downstream of the cylinder (about $9.5D$ for the fine resolution).

Table C.10: Mesh parameters for the NW solver alone in the shedding case at $Re = 200$.

$N_n \times N_\theta$	w/R	$R/h_{\mathrm{NW}}^{n,\mathrm{wall}}$	$h_{\mathrm{NW}}^{\theta,\mathrm{wall}}/h_{\mathrm{NW}}^{n,\mathrm{wall}}$	h_{i+1}^n/h_i^n
1101×1600	80	250	$\simeq 1$	$\simeq 1.004$

References

[1] G. S. Winckelmans, Vortex Methods, in: Encyclopedia of Computational Mechanics, volume 3, 2nd ed., John Wiley & Sons, Ltd, 2004, pp. 129–153. doi:10.1002/0470091355.ecm055.

[2] G.-H. Cottet, P. D. Koumoutsakos, et al., Vortex methods: theory and practice, volume 8, Cambridge University Press, 2000.

[3] D.-G. Caprace, P. Chatelain, G. Winckelmans, Wakes of rotorcraft in advancing flight: A large eddy simulation study, Physics of Fluids 32 (2020) 087107.

[4] R. E. Brown, A. J. Line, Efficient high-resolution wake modeling using the vorticity transport equation, AIAA journal 43 (2005) 1434–1443.

[5] D. Rossinelli, B. Hejazialhosseini, W. van Rees, M. Gazzola, M. Bergdorf, P. Koumoutsakos, Mrag-i2d: Multi-resolution adapted grids for remeshed vortex methods on multicore architectures, Journal of Computational Physics 288 (2015) 1–18.

[6] P. Koumoutsakos, A. Leonard, F. Pepin, Boundary conditions for viscous vortex methods, Journal of Computational Physics 113 (1994) 52–61.

[7] P. Ploumhans, G. Winckelmans, Vortex methods for high-resolution simulations of viscous flow past bluff bodies of general geometry, Journal of Computational Physics 165 (2000) 354–406.

[8] D. Milani, G. Morgenthal, Methods for controlling the local spatial and temporal resolution of vortex particle simulations of bluff body aerodynamics problems, Computers & Fluids 166 (2018) 225 – 242.

[9] G. Morgenthal, J. H. Walther, An immersed interface method for the vortex-in-cell algorithm, Computers & Structures 85 (2007) 712–726.

[10] M. Coquerelle, G. H. Cottet, A vortex level set method for the two-way coupling of an incompressible fluid with colliding rigid bodies, Journal of Computational Physics 227 (2008) 9121–9137.

[11] M. Gazzola, P. Chatelain, W. M. van Rees, P. Koumoutsakos, Simulations of single and multiple swimmers with non-divergence free deforming geometries, Journal of Computational Physics 230 (2011) 7093–7114.

[12] T. Gillis, G. Winckelmans, P. Chatelain, An efficient iterative penalization method using recycled krylov subspaces and its application to impulsively started flows, Journal of Computational Physics 347 (2017) 490–505.

[13] C. Bernier, M. Gazzola, R. Ronsse, P. Chatelain, Simulations of propelling and energy harvesting articulated bodies via vortex particle-mesh methods, Journal of Computational Physics 392 (2019) 34–55.

[14] T. Gillis, Y. Marichal, G. Winckelmans, P. Chatelain, A 2D immersed interface vortex particle-mesh method, Journal of Computational Physics 394 (2019) 700–718.

[15] M. L. Ould-Salihi, G.-H. Cottet, M. El Hamraoui, Blending finite-difference and vortex methods for incompressible flow computations, SIAM Journal on Scientific Computing 22 (2001) 1655–1674.

[16] G. Cottet, Particle-grid domain decomposition methods for the navier-stokes equations in exterior domains, Lectures in Applied Mathematics 28 (1991) 103–117.

[17] J.-L. Guermond, H. Lu, A domain decomposition method for simulating advection dominated, external incompressible viscous flows, Computers & Fluids 29 (2000) 525 – 546.

[18] G. Daeninck, Developments in hybrid approaches. Vortex method with known separation location. Vortex method with near-wall Eulerian solver. RANS-LES coupling, Ph.D. thesis, Université catholique de Louvain, 2006.

[19] Y. Marichal, An immersed interface vortex particle-mesh method, Ph.D. thesis, Université catholique de Louvain, 2014.

[20] M. Stock, A. Gharakhani, C. Stone, Modeling Rotor Wakes with a Hybrid OVERFLOW-Vortex Method on a GPU Cluster, American Institute of Aeronautics and Astronautics, 2010. doi:doi:10.2514/6.2010-4553.

[21] A. J. Chorin, Numerical solution of the navier-stokes equations, Mathematics of computation 22 (1968) 745–762.

[22] J. Kim, P. Moin, Application of a fractional-step method to incompressible navier-stokes equations, Journal of computational physics 59 (1985) 308–323.

[23] M. J. Lee, B. Do Oh, Y. B. Kim, Canonical fractional-step methods and consistent boundary conditions for the incompressible navier–stokes equations, Journal of computational physics 168 (2001) 73–100.

[24] S. Balay, W. D. Gropp, L. C. McInnes, B. F. Smith, Efficient management of parallelism in object oriented numerical software libraries, in: E. Arge, A. M. Bruaset, H. P. Langtangen (Eds.), Modern Software Tools in Scientific Computing, Birkhäuser Press, 1997, pp. 163–202.

[25] S. Balay, S. Abhyankar, M. F. Adams, J. Brown, P. Brune, K. Buschelman, L. Dalcin, A. Dener, V. Eijkhout, W. D. Gropp, D. Karpeyev, D. Kaushik, M. G. Knepley, D. A. May, L. C. McInnes, R. T. Mills, T. Munson, K. Rupp, P. Sanan, B. F. Smith, S. Zampini, H. Zhang, H. Zhang, PETSc Web page, https://www.mcs.anl.gov/petsc, 2019. URL: https://www.mcs.anl.gov/petsc.

[26] P. Chatelain, A. Curioni, M. Bergdorf, D. Rossinelli, W. Andreoni, P. Koumoutsakos, Billion vortex particle Direct Numerical Simulations of aircraft wakes, Computer Methods in Applied Mechanics and Engineering 197 (2008) 1296–1304.

[27] J. Monaghan, Extrapolating B splines for interpolation, Journal of Computational Physics 60 (1985) 253 – 262.

[28] R. Hockney, J. Eastwood, Computer Simulation Using Particles, Taylor & Francis, Inc., Bristol, PA, USA,, 1988.
[29] P. Chatelain, P. Koumoutsakos, A fourier-based elliptic solver for vortical flows with periodic and unbounded directions, Journal of Computational Physics 229 (2010) 2425–2431.
[30] D.-G. Caprace, T. Gillis, P. Chatelain, Flups: A fourier-based library of unbounded poisson solvers, SIAM Journal on Scientific Computing 43 (2021) C31–C60.
[31] F. Noca, D. Shiels, D. Jeon, A comparison of methods for evaluating time-dependent fluid dynamic forces on bodies, using only velocity fields and their derivatives, Journal of Fluids and Structures 13 (1999) 551–578.
[32] P. Koumoutsakos, A. Leonard, High-resolution simulations of the flow around an impulsively started cylinder using vortex methods, Journal of Fluid Mechanics 296 (1995) 1–38.
[33] W. Collins, S. Dennis, The initial flow past an impulsively started circular cylinder, The Quarterly Journal of Mechanics and Applied Mathematics 26 (1973) 53–75.
[34] R. D. Blevins, Flow-induced vibration: 2nd edition (1990).
[35] J. A. Wright, R. W. Smith, An edge-based method for the incompressible navier–stokes equations on polygonal meshes, Journal of Computational Physics 169 (2001) 24–43.
[36] M. Rosenfeld, D. Kwak, M. Vinokur, A fractional step solution method for the unsteady incompressible navier–stokes equations in generalized coordinate systems, Journal of Computational Physics 94 (1991) 102–137.
[37] J.-I. Choi, R. C. Oberoi, J. R. Edwards, J. A. Rosati, An immersed boundary method for complex incompressible flows, Journal of Computational Physics 224 (2007) 757–784.
[38] G. Y. Dynnikova, Y. A. Dynnikov, S. Guvernyuk, Mechanism underlying Kármán vortex street breakdown preceding secondary vortex street formation, Physics of Fluids 28 (2016) 054101.
[39] J. M. Cimbala, H. M. Nagib, A. Roshko, Large structure in the far wakes of two-dimensional bluff bodies, Journal of Fluid Mechanics 190 (1988) 265–298.
[40] T. Gillis, W. M. van Rees, A scalable computational framework for wavelet-based multiresolution grids, in: SIAM Conference on Computational Science and Engineering (CSE21), 2021.
[41] G. K. Batchelor, An introduction to fluid dynamics, Cambridge University Press, 1967.
[42] R. A. Adams, C. Essex, Calculus: a complete course, Seventh Edition, Pearson Addison Wesley, 2010.